Catalysis Today 160 (2011) 116–130

Contents lists available at ScienceDirect

Catalysis Today

journal homepage: www.elsevier.com/locate/cattod

# Size-dependent selectivity and activity of silver nanoclusters in the partial oxidation of propylene to propylene oxide and acrolein: A joint experimental and theoretical study

Luis M. Molina[a,1], Sungsik Lee[b,1], Kristian Sell[c,1], Giovanni Barcaro[d,1], Alessandro Fortunelli[d,1], Byeongdu Lee[b], Soenke Seifert[b], Randall E. Winans[b], Jeffrey W. Elam[e], Michael J. Pellin[f], Ingo Barke[c], Viola von Oeynhausen[c], Yu Lei[f,g], Randall J. Meyer[g], Julio A. Alonso[a], Arantxa Fraile Rodríguez[h,2], Armin Kleibert[h], Suzanne Giorgio[i], Claude R. Henry[i], Karl-Heinz Meiwes-Broer[c], Stefan Vajda[f,j,k,*]

[a] Departamento de Física Teórica, Atómica y Óptica, Universidad de Valladolid, 47011 Valladolid, Spain
[b] X-ray Sciences Division, Argonne National Laboratory, 9700 South Cass Avenue, Argonne, IL 60439, USA
[c] Institut für Physik, Universität Rostock, Universitätsplatz 3, D-18051 Rostock, Germany
[d] Molecular Modeling Laboratory, IPCF-CNR, Via Giuseppe Moruzzi 1, Pisa I56124, Italy
[e] Energy Systems Division, Argonne National Laboratory, 9700 South Cass Avenue, Argonne, IL 60439, USA
[f] Materials Science Division, Argonne National Laboratory, 9700 South Cass Avenue, Argonne, IL 60439, USA
[g] Department of Chemical Engineering, University of Illinois at Chicago, 810 South Clinton Street, Chicago, IL 60607, USA
[h] Swiss Light Source, Paul Scherrer Institut, CH-5232 Villigen PSI, Switzerland
[i] CINaM-CNRS and Aix-Marseille Université, Campus de Luminy, Case 913, 13288 Marseille, Cédex 09, France
[j] Center for Nanoscale Materials, Argonne National Laboratory, 9700 South Cass Avenue, Argonne, IL 60439, USA
[k] Department of Chemical Engineering, Yale University, 9 Hillhouse Avenue, New Haven, CT 06520, USA

ARTICLE INFO

*Keywords:*
Silver clusters
Propene
Propylene
Propylene oxide
Acrolein
Density-functional calculations
Oxametallacycle complex
Cluster reshaping

ABSTRACT

Model silver nanocatalysts between 9 and 23 nm in size were prepared by size-selected cluster deposition from a free cluster beam on amorphous alumina films and their size-dependent catalytic performance studied in the partial oxidation of propylene under realistic reaction conditions. Smaller clusters preferentially produced acrolein, while the 23 nm particles were considerably more selective towards the formation of propylene oxide, at reaction rates far exceeding those previously reported for larger silver particles. The activity of clusters dropped significantly with increasing particle size. First-principle calculations, of the activation energies for oxygen adsorption and its dissociation, at variable surface coverage yielded surface energies which resulted in particle shapes resembling the experimentally observed shapes of partially oxidized silver clusters. The calculated activation barriers for propylene oxide and acrolein formation on various facets and on the edges of the nanoparticles provided detailed information about the energetics of the competing reaction pathways. The size- and corresponding morphology dependent theoretical activity and selectivity are in good accord with experimental observations.



## 1. Introduction

Propylene oxide (PO) and acrolein (Acr) are important precursors for a variety of commodity chemicals [1]. Traditional processes to produce propylene oxide are energy-intensive, inefficient and environmentally unfriendly since the processes involve multiple steps and create large quantities of by-products and waste. Therefore, the heterogeneously catalyzed direct oxidation of propylene by molecular oxygen has received increased attention [1–9]. Silver-based catalysts have been successfully used in the epoxidation of ethylene on both the laboratory [3] and industrial scale [10], but no viable catalyst for propylene epoxidation has been identified that would use molecular oxygen. Much of the effort so far has been centered on the nature of the active oxygen species [11] and size-dependent selectivity and reactivity [2]. However, the use of silver in propylene epoxidation has been hampered by either low conversion or poor selectivity towards propylene oxide. Moreover, to date a detailed atomic level understanding of this process is still lacking [2,5,8,9,12].

* Corresponding author at: Argonne National Laboratory, Materials Science Division and Center for Nanoscale Materials, 9700 S Cass Avenue, Building 200, Room A109, Argonne, IL 60439, USA. Tel.: +1 630 252 8123; fax: +1 630 252 4954.
*E-mail address:* vajda@anl.gov (S. Vajda).
[1] Equally contributing (first) authors.
[2] Current address: Departament de Física Fonamental i Institut de Nanociència i Nanotecnologia, Universitat de Barcelona, E-08027 Barcelona, Spain.

0920-5861/$ – see front matter © 2010 Elsevier B.V. All rights reserved.
doi:10.1016/j.cattod.2010.08.022

In the case of heterogeneous catalysts dispersed on supports, it is a challenging task to elucidate the structure–reactivity relationship with the traditional catalyst preparation methods which introduce variations in mean particle size and particle size distribution. Therefore, size-selected cluster deposition methods are well positioned to contribute to the understanding of the effect of catalyst particle size on its catalytic reactivity and selectivity by providing highly uniform supported model catalyst systems for such studies [13–29]. In general, the activity of the catalytic metals can be optimized when used in a form of small sub-nanometer clusters or small nanoparticles [15,19,26,27,30–42]. In the epoxidation of propylene to propylene oxide on silver and gold nanoparticles these catalysts exhibit strongly size-dependent catalytic activity and selectivity [2,7,43,44]. However, none of the nanometer sized catalysts reported to date possess both high conversion and selectivity towards propylene oxide. For example, Haruta and co-workers discovered a highly selective propylene epoxidation catalyst based on titania-supported 2–4 nm gold nanoparticles when hydrogen is co-fed with the oxygen and propylene mixture [7]. However, the selectivity of these gold nanoparticles is extremely sensitive to their size and shape, with particles smaller than 1.5–2.0 nm mainly producing propane and particles larger than 4–5 nm preferentially catalyzing oxidation of propylene to $CO_2$ and $H_2O$. Size-preselected sub-nanometer gold clusters stabilized on amorphous alumina exhibit highly selective catalysis for this reaction [23], while sub-nanometer Ag clusters and their aggregates possess high activity [25]. In order to make a correlation between the shape/morphology of the catalyst and its function, it is necessary to track changes in nanoparticle shape induced by temperature and exposure to reactive gases *in situ*, under realistic reaction conditions. In the present study, grazing incidence small-angle X-ray scattering (GISAXS) [22,24,44–46] was used to monitor the change in size and shape of supported silver nanoparticles, while the catalytic performance was followed simultaneously by temperature-programmed reaction (TPRx) under atmospheric pressure.

On the theoretical side, modern developments in computational software and hardware allow one to investigate adsorption mechanisms and elementary reaction steps on realistic metal systems, and studies have been conducted on the oxidation of extended Ag surfaces and the interaction of alkenes with both bare and oxidized Ag substrates in previous work [47–56]. For oxygen adsorption on the (1 0 0) surface, a close competition has been found between oxygen-induced reconstruction and simple oxygen chemisorption in hollow sites [47] and it has been shown that at medium/high oxygen coverage the formation of subsurface oxygen species is energetically favoured. In contrast, alkenes bind rather weakly on bare extended silver surfaces, mainly through the interaction of the $\pi$ orbitals of the organic species with the *d* orbitals of the metal atoms [49], even though the binding energy can increase in the proximity of extended defects (steps) and adatoms [50,51]. Co-adsorption with oxygen promotes the interaction of alkenes. Chemisorbed oxygen adatoms interact with olefinic molecules giving rise to oxametallacycle intermediates [52] which act as precursors for the formation of epoxide or aldehyde species, while surface reconstructions induced by subsurface oxygen atoms produce an increase of the interaction energy of ethylene molecules with the surface due to a *push-out* effect [48]. The formation of $\pi$-bonded olefinic species and oxametallacycle intermediates has been shown to take place also on the silver (1 1 1) surface [53]. The involved bonding mechanisms are similar to those on the (1 0 0) surface in the case of mild oxidation with the formation of chemisorbed species. At high temperature (above 100 °C) in an oxygen atmosphere the (1 1 1) surface reconstructs with the formation of mixed silver–oxygen phases [54–56], and the formation of oxametallacycle intermediates can occur as well due to the presence of surface oxygen atoms [54].

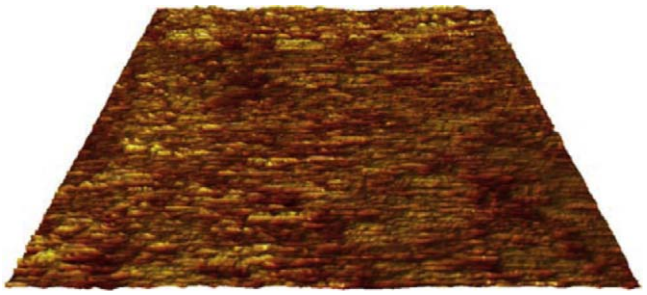

**Fig. 1.** Topographic STM image of the amorphous alumina support layer (500 nm × 500 nm, $U_T = -1.8$ V, $I_T = -0.5$ nA). The RMS roughness is about 0.69 nm.

In the present joint experimental and theoretical work, a study of the catalytic activity and selectivity of size-selected silver clusters of 9–23 nm size in the direct partial oxidation of propylene using molecular oxygen to preferentially produce propylene oxide and acrolein was undertaken. The very strong effect of size on catalyst performance is presented, along with the evolution of the morphology of the catalyst under reaction conditions. Accompanying first-principle simulations are then used to clarify the adsorption and reaction mechanisms of oxygen and alkene species on extended silver surfaces and finite-size models. Theoretical studies, here supplement prior results and explore cluster reshaping under realistic conditions. The cooperative effects in surface/oxygen/alkene interaction are investigated and compared with experimental results on nanometer clusters. Differences in the structural features of the nanometer sized silver clusters between room temperature and 200 °C are highlighted, focusing in particular on the presence and availability of reactive oxygen species, and are used to set up models providing a coherent mechanistic framework for the restructuring of clusters and its influence on selectivity, which is in excellent agreement with the experimental catalytic data.

## 2. Experimental methods

### 2.1. Support preparation: atomic layer deposition of thin amorphous alumina films

Atomic layer deposition (ALD) was used to deposit the alumina support layer on top of a naturally oxidized silicon wafer. ALD is a thin film growth technique that uses alternating cycles of saturating reactions between gaseous precursor molecules and the surface of the substrate to deposit films. In the case of $Al_2O_3$ it uses alternating exposures to trimethyl aluminum (TMA) and water [57]:

$$Al{-}OH* + Al(CH_3)_3 \rightarrow Al{-}O{-}Al(CH_3)_2* + CH_4 \quad (1)$$

$$Al{-}CH_3* + H_2O \rightarrow Al{-}OH* + CH_4 \quad (2)$$

The asterisks represent surface species, and the reactions have been simplified to show only a single functional group. In Eq. (1), the surface hydroxyl species OH* reacts with TMA to attach methyl-terminated Al atoms and liberate methane gas. In Eq. (2), the resulting $-CH_3$* surface groups react with water to restore the hydroxyl-termination and again liberate methane. In an iterative fashion, films of well-controlled thickness can be grown. In this study, six ALD cycles were used to coat the silicon. The thickness of the ALD $Al_2O_3$ layer was 7.2 Å based on a growth rate of 1.2 Å per cycle determined by spectroscopic ellipsometry. From the known density of ALD $Al_2O_3$ of 3.0 g/cm$^3$, we estimate a monolayer thickness of 3.0 Å so that the $Al_2O_3$ used in this study had a thickness of 2–3 monolayers. With a scanning tunneling microscope (Omicron LT-STM) the rough and amorphous surface of the created support layer was revealed (Fig. 1). The surface roughness of about

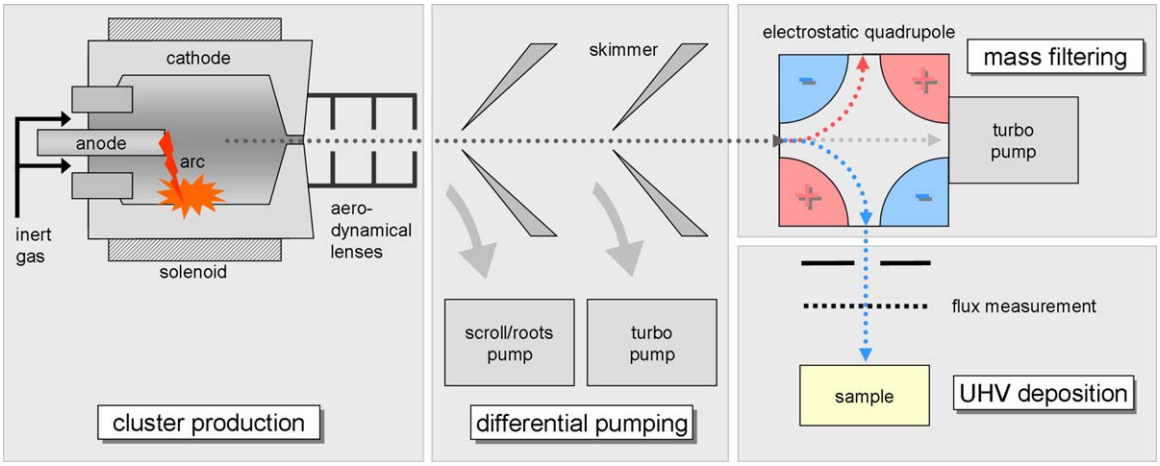


**Fig. 2.** Schematic view of the arc cluster ion source (ACIS) used for cluster production and deposition.

0.69 nm (RMS) is to be viewed as a lower limit due to convolution effects with the tip geometry. Uniform appearance and absence of large protrusions are characteristics of the substrates. Much of the roughness arises from the incomplete second monolayer. Supporting low energy electron diffraction (LEED) investigations showed no evidence of a periodic crystal structure at the sample surface.

### 2.2. Size-selected cluster deposition

Deposition of Ag clusters was performed in Rostock using an arc cluster ion source (ACIS) that is connected to a ultrahigh vacuum (UHV) preparation chamber [18]. The clusters are deposited from the free beam onto a flat 10 mm × 10 mm substrate produced by ALD as described above.

The wafers are transferred into the UHV chamber with a load-lock system and positioned in front of the ACIS. The schematic set-up of the deposition process is shown in Fig. 2.

In a cylindrical Ag cathode an arc is ignited between the water-cooled anode and the target-material. As a result, metal-vapor plasma is formed in the high temperature area. The cluster aggregation takes place in an inert gas atmosphere of about 80% He and 20% Ar with a total pressure of about 3 kPa within the cathode. Around the cathode a solenoid is mounted to ensure a rotation of the arc so that the cathode is eroded uniformly in all radial directions. The cluster beam passes an expansion channel, a system of aerodynamical lenses [58] and two skimmers where it is separated from the large part of the rare gas. An electrostatic quadrupole is used to deflect the charged clusters by 90° and to select the particle size. The latter is adjusted by the voltage applied to the four quadrupole plates. For this work voltages between 100 and 2000 V are used for sizes between 9 and 23 nm. The cluster current measured at a highly transparent metal grid is proportional to the cluster flux at the location of the sample. It has been calibrated for various cluster sizes by determining the cluster density utilizing TEM. One main challenge during deposition is to reduce the gas pressure from $2.96 \times 10^{-2}$ atm in the cathode to UHV conditions at the support to obtain pure and well-defined particle deposits [58,59]. Several differential pumping stages are used for this purpose as shown in Fig. 2. For cluster sizes used in this work the kinetic energy per atom is less than 20 meV which is estimated based on a spherical cluster shape with measured cluster diameters. These energies are well within the regime of soft-landing conditions observed experimentally [60,61] and obtained from simulations [62,63]. Since no fragmentation or implantation takes place under such conditions, the number of atoms is not expected to change upon deposition. The absence of fragments was confirmed by scanning electron microscopy. The particles therefore maintain their gas-phase size and shape, but may experience a flattening upon impact and with interaction with the substrate [64]. The deposition process further leads to a random orientation of particles in the present size range [65]. For the sample coverage a cluster density of about $10^8$ clusters per $cm^2$ was applied to avoid particle aggregation upon landing. As determined by scanning electron microscopy and X-ray scattering (see below for details), the lateral diameter of the supported size-selected clusters was around 9, 12 and 23 nm on the three samples, respectively.

### 2.3. Scanning electron microscopy

After the deposition process the samples were transferred to air and transported to scanning electron microscopy (SEM) at the Paul Scherrer Institut to determine the lateral diameter and number of clusters on the support before they continued to the Advanced Photon Source at Argonne National Laboratory for X-ray scattering and reactivity studies. After the reactivity studies, the samples were sent back to the Paul Scherrer Institut for SEM in order to verify particle size after the reactivity studies. The high resolution SEM measurements were performed on a Zeiss FE-SEM Supra VP55 apparatus.

### 2.4. In situ high-resolution environmental transmission electron microscopy

For the *in situ* observation in a high-resolution environmental transmission electron microscopy (HRETEM) at CINaM Marseille, the silver clusters were directly deposited on special copper discs covered with a transparent 6–8 nm thick carbon film. The copper discs had a diameter of 3 mm and were pierced at the center by 7 adjacent holes of 0.15 mm in diameter in a hexagonal arrangement. With a continuous carbon film covering the pierced area, the discs are gas proof and were tested up to a pressure difference of $3.95 \times 10^{-1}$ atm on each side before use. The samples were mounted in a closed environmental TEM sample holder from JEOL, described in details in previous work [66,67]. This sample holder can be used with a standard microscope (JEOL 3010) equipped with a large gap pole piece (Cs = 1.4 mm). Under these conditions, the point resolution is 0.21 nm. A similar copper disc with a clean carbon film was used to close the sample holder. The clusters were sandwiched between the two carbon films; the gas was circulated between the carbon films at the level of the sample. In this simple closed environmental cell, the gas pressure must be lower than $2.96 \times 10^{-2}$ atm at room temperature. In this work, sil-

ver clusters were imaged at room temperature and a gas pressure of $3.95 \times 10^{-3}$ atm in pure $H_2$ and pure $O_2$. The images were recorded with a fast CCD camera to minimize exposure times. In order to reduce undesired effects caused by the electron beam, which after long exposures can cause a degradation of the sample, the adjustments of the electron beam optics were done on different areas than the working area of interest.

### 2.5. Grazing incidence small-angle X-ray scattering

Grazing incidence small-angle X-ray scattering (GISAXS) has been proved to be very powerful to study particles at surfaces and their transformations under vacuum conditions and low-pressure reactive gas environments at the nanometer [24,25,44,45,68–71] and sub-nanometer scale [22,23,25,41,72]. In addition to the determination of the size and shape of clusters, GISAXS can also provide information about faceting of nanoparticles [44,71] and structure of fractals [73,74]. The GISAXS experiments were performed at the 12-ID-C beamline of the Advanced Photon Source using X-rays of 12.0 keV energy in a reaction cell of our own design. The internal volume of the cell is approximately 25 ml, with the sample mounted on a ceramic heater in the center of the cell. The cell was sealed with mica windows and mounted on a computer controlled goniometer and equipped with gas feedthroughs mounted in the side walls of the cell. The reactant gas mixture was premixed in a remotely controlled gas-mixing unit with calibrated mass flow controllers (Brooks model SLA5850). The reaction temperature was controlled using a ceramic heater, and the sample temperature measured with a K-type thermocouple attached to the edge of the heater surface. As shown in Fig. 3, the X-ray beam was scattered off the surface of the sample at near the critical angle ($\alpha_c = 0.18^\circ$) of the substrate. A $1024 \times 1024$ pixel two-dimensional MarCCD detector was used for recording the GISAXS images from the sample. GISAXS data were collected as a function of reaction temperature and time. The two-dimensional X-ray images were analyzed by taking cuts in the $q_y$ direction for horizontal information and in the $q_z$ direction for vertical information. Scattering vectors $q$ are calculated from $(4\pi/\lambda)\sin\theta_f$ where $\theta_f$ is the scattering half angle and $\lambda$ is the wavelength of the X-rays. The data were analyzed by Guinier analysis [75], providing the horizontal and vertical particle radii of gyration $R_{gH}$ and $R_{gV}$, respectively. The diameter and height of the nanoparticles can be calculated from the radii of gyration as $2.58 \times R_{gH}$ and $R_{gV}$, respectively. The uncertainty in the particle size was estimated to be ±0.2 nm or better, which is 2% of the particle size or less. In this

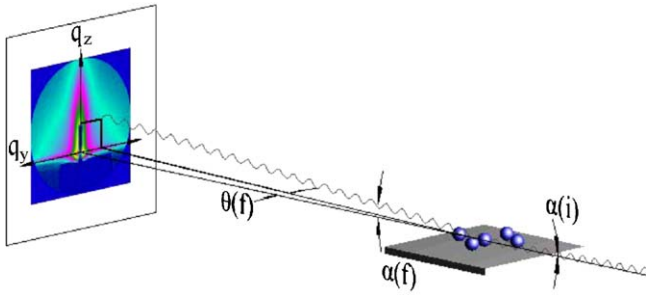


**Fig. 3.** The schematic of the GISAXS experiment: incident angle $\alpha_i = 0.18^\circ$ and scattered beam angle $\alpha_f$.

study, GISAXS was used to determine the diameter of clusters size under vacuum conditions before and after the reaction as well as to monitor changes in particle morphology under reaction conditions.

### 2.6. Temperature-programmed reaction

The catalytic tests were performed in the reaction cell designed for the GISAXS experiments (see above) using temperature-programmed reaction (TPRx) at 1.3 atm pressure and total gas flow of 30 sccm. To achieve thermal equilibrium between the heater and sample during the application of a temperature ramp, a low heating rate (<1.5 °C/min.) was used. The gas mixture used consisted of 0.67% $C_3H_6$ and 0.33% $O_2$ in helium. The reaction products were analyzed on a differentially pumped quadrupole mass spectrometer (Pfeiffer Prisma). $m/z = 58$ was chosen to monitor the propylene oxide, as has been used by several other groups [76–79]. Theoretical and experimental work has shown that during the oxidation of propylene a variety of partial oxidation products can in principle form, some of which having the same molecular formula and mass as propylene oxide (the parent ions of acetone and propenol also have $m/z = 58$), a careful analysis of the mass spectra of the gas mixture exiting from the reaction cell was performed. Based on fragment patterns of the NIST mass spectra of these species the formation of acetone and propenol could be excluded based on the following. For the on-line analysis of the gas mixture exiting from the reaction cell during the course of the reaction, the mass spectrometer was operated in multi-ion-detection mode (MID). This operation mode allows for a simultaneous monitoring of the ion current corresponding to up to 24 $m/z$ values. In our experiments a

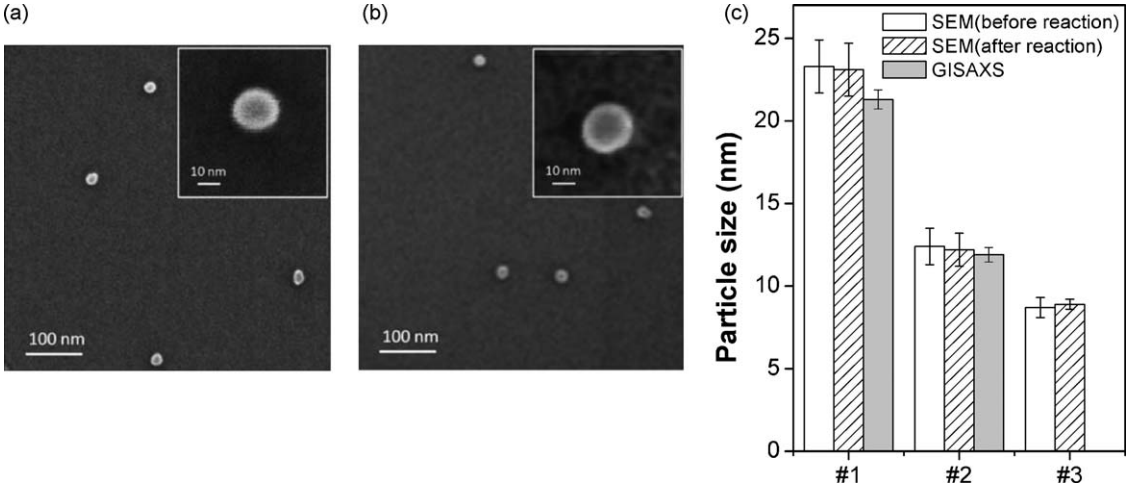


**Fig. 4.** Representative HRSEM images of silver nanoclusters of 23.3 nm (sample #1) in size (a) before the epoxidation reaction and (b) after reaction cycles. (c) Particle lateral size and size distribution (indicated by bars) at room temperature from SEM images before and after the reaction, and average lateral diameter and uncertainty from data fitting (error bars) from GISAXS before reaction (average sizes #1 = 23.3 nm, #2 = 12.0 nm, #3 = 8.7 nm).

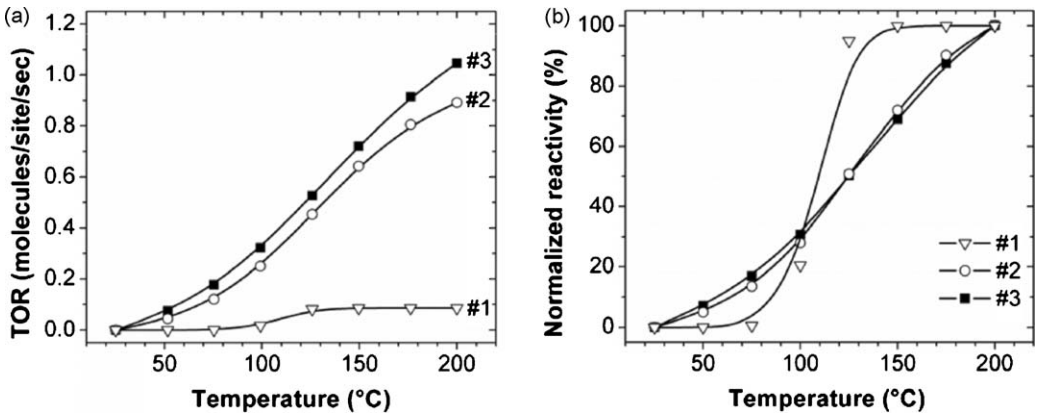


**Fig. 5.** (a) Background-corrected temperature dependent per surface atom turn-over rate of propylene oxide formation in the partial oxidation of propylene for three cluster sizes. (b) Normalized TORs of propylene oxide as a function of temperature (average lateral diameter of clusters: #1 = 23.3 nm, #2 = 12 nm, #3 = 8.7 nm). The signals plotted are background-corrected ones, using a support of the same size and composition without catalytic particles, and tested under identical conditions as the catalyst-containing sample. The background ion signal intensity for propylene oxide measured on a blank alumina support were below 4% of the signal intensity measured in the presence of silver nanoclusters, respectively. The mass spectrometer was calibrated using certified gas mixtures of the reactants and products in balance helium gas under identical flow conditions as in the TPRx experiments.

total of 20 $m/z$ values were monitored, including the $m/z$ values corresponding to the mass peaks of acetone and propenol, leading to the following conclusions: (1) propenol could be excluded because the mass spectrometer's MID signal corresponding to $m/z = 57$, the major peak of propenol, was below the detection limit during the entire temperature-programmed reaction cycle. Acetone could be excluded because there was no change in the mass spectrometer signal (MID) corresponding to $m/z = 43$, the major peak of acetone [80]. The uncertainty in the mass spectrometer signal has been estimated from standard deviation of 11–23 readout points which includes points both below and above the plotted reaction temperature. The uncertainty is estimated to be ~2% of the ion current. Taking into consideration an estimated 10% uncertainty in the determination of the number of deposited atoms, the uncertainty in determination of the turn-over rates is estimated to be about 10% of the reported values. This approach is analogous to the one reported by the Anderson group [81].

An estimate of the number of accessible surface silver atoms to the reactants was done by assuming hemispherical particle shape for the supported particles, with the lateral diameter and aspect ratio determined by SEM and GISAXS. The exposed surface area of the particles was calculated from the average height and diameter of particles. (This excluded the Ag atoms sitting on the alumina support which were inaccessible to the reactant molecules.) The number of accessible atoms of the hemisphere was calculated by taking into consideration the 2.88 Å Ag–Ag distance in Ag(1 1 1) with a fcc structure [82].

## 3. Computational methods

Density-functional (DF) calculations on the oxidation of Ag surfaces were performed using the QuantumEspresso computational code [83], employing ultrasoft pseudopotentials [84] and the Perdew, Burke, and Ernzerhof (PBE) [85] exchange-correlation functional. Values of 40 and 240 Ryd were employed as the energy cut-offs for the selection of the plane wave basis set for the description of the wave-function and the electronic density, respectively. DF calculations were performed spin-polarized by applying a Gaussian smearing technique with a broadening of the one-particle levels of 0.03 eV. To describe the silver surfaces, a supercell approach with a 7-layer metal slab was employed. To describe oxygen adsorption at increasing coverage, $(3 \times 3)$ and $(2 \times 2)$ cells were used; namely the $(3 \times 3)$ cell has been used in the case of 1/9 coverage, whereas the $(2 \times 2)$ cell for 1/4 and 1/2 coverages. A (4 4 1) k-grid was used to sample both the $(2 \times 2)$ and the $(3 \times 3)$ cells. In the case of the (1 1 0) surface, where the two in-plane lattice vectors of the unit cell do not have the same length, we have adopted a (4 3 1) k-grid. The silver atoms were positioned at the crystal sites of the fcc structure at a first-neighbour distance of 2.947 Å, corresponding to the equilibrium value predicted for fcc silver by our DF/PBE approach. The inner three layers were kept fixed in the crystal positions, whereas the outer two were allowed to relax. A symmetric adsorption on both sides of the metal slab was adopted to cancel the dipole moment developed by the adsorption process. Empty space between replicated cell was chosen between 10 and 15 Å.

The DF calculations for the partial oxidation of propylene were carried out using the DACAPO code [86], which also employs ultrasoft pseudopotentials. The set-up is slightly different: the PW91 functional [87] was used for exchange-correlation, and in order to keep the computational cost low (due to the large number of simulations which these type of studies of reaction pathways requires) the energy cut-off for the plane wave basis was slightly lower (25 Ryd). For the same reason, the Ag(1 1 1) surface was modeled using a 3-layer metal slab (relaxing only the first layer). Energy barriers were calculated by a constrained minimization method, involving several simulations where the reaction coordinate (C–O or C–H bond distance) was restricted at increasingly smaller values, while allowing the rest of the system to freely relax [88].

## 4. Experimental results and discussion

### 4.1. Characterization of the size of the supported clusters by SEM and GISAXS

Representative SEM images obtained on a silver sample before and after reaction are shown in Fig. 4a and b, respectively. The average lateral diameter of the clusters is determined by using the *Scion Image* software. The error bar is the standard deviation of the corresponding particle size counted from several SEM images on different areas of the given sample. The samples #1, #2 and #3 consisted of discrete silver clusters with an average size of 23.3, 12 and 8.7 nm, respectively, with a very narrow size distribution (<5%) as shown with bars in Fig. 4c. No noticeable change is observed in the mean cluster size and its distribution before and after the reaction. Cluster lateral diameters determined by GISAXS for samples #1 and #2 are also very well matched with SEM results. The density of the silver particles on sample #3 is too low for accu-

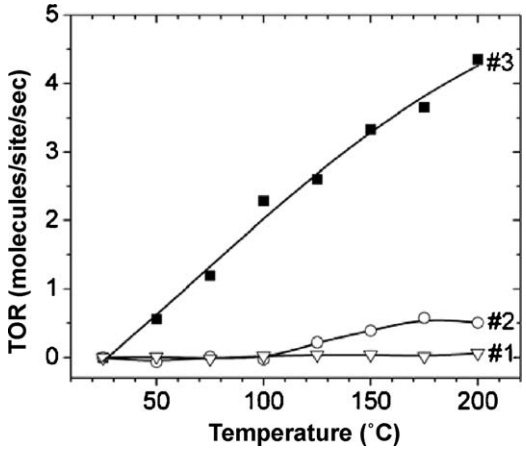


**Fig. 6.** Background-corrected temperature dependent per surface atom turn-over rate of acrolein formation in the partial oxidation of propylene for three silver cluster sizes (average lateral diameter #1 = 23.3 nm, #2 = 12 nm, #3 = 8.7 nm). The background ion signal intensity for acrolein measured on a blank alumina support was below 15% of the signal intensities measured in the presence of the silver clusters.

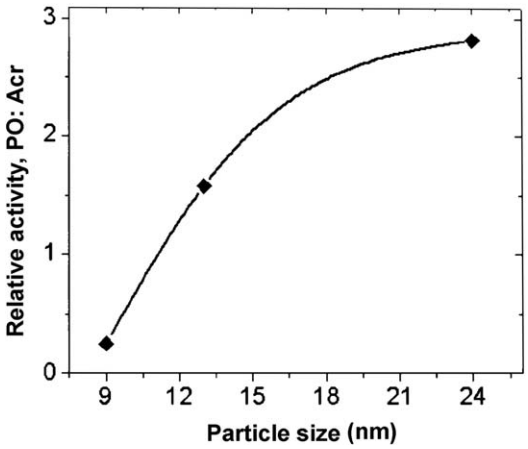


**Fig. 7.** Selectivity of silver catalyst (ratio propylene oxide/acrolein) at 200 °C as the function of particle size.

rate GISAXS measurements. Cluster lateral diameters and heights are determined from the Guinier analysis of the GISAXS images collected at room temperature under pure helium. The results show an average aspect ratio of about 1.6. The uncertainty of the dimensions obtained by the analysis of the GISAXS data (~0.2 nm) is calculated based on the counting statistics, which provides errors of data fitting (linear regression in this case). As discussed in detail in Ref. [24], the aspect ratio of the silver nanoclusters undergoes dramatic changes after the exposure of the particles to the reactant gas mixture and further evolves with temperature. Similar changes were observed for the smaller cluster sizes reported here.

The alumina-supported silver nanoclusters are very stable catalysts—they retain their size over the course of 4–6 reaction hours, as determined by GISAXS and by the analysis of SEM images collected before and after the reaction cycles (see Fig. 4a and b). Thus we could exclude both aggregation and Ostwald ripening [89] under our reaction conditions for all three particle sizes—an important aspect in the light of potential future applications.

### 4.2. TPRx: size-dependent activity and selectivity

Fig. 5a shows turn-over rates (TOR) of propylene oxide formation per surface atom on various size silver cluster catalysts. The smaller size silver clusters #2 and #3 (12 and 8.7 nm lateral diameter, respectively) start to react at much lower temperature than the largest particles #1 (23.3 nm); the latter start to show catalytic activity at ~80 °C and reaching maximum activity at ~150 °C [24]. At temperatures above 100 °C, the smaller silver clusters #2 and #3 exhibit about an order of magnitude higher reactivity than the largest size clusters #1. These results, along with the comparison of the trends exhibited by the normalized TORs (Fig. 5b) indicate that the reaction mechanism may change when crossing the ~20 nm size range.

It should be noted that 100 °C is reported to be the required temperature to form subsurface oxygen in silver via dissociation of molecular oxygen, which plays important role on extended silver surfaces [90–92], and Lu et al. identified an increased $Ag_2O$ phase with decreasing particle size during the epoxidation of ethylene [5]. As reported by Savio et al. [93] in their study of $O_2$ adsorption at stepped surfaces, open steps favour the dissociation of oxygen and provide a gateway through which subsurface sites can be accessed.

Fig. 6 shows the turn-over rate of the acrolein, the main co-product identified, as a function of reaction temperature. High reactivity towards acrolein formation, about 4 times of propylene oxide production, is observed on smallest size clusters #3 (8.7 nm). The rate of acrolein production sharply decreases with increasing cluster size, dropping to about 1/3 of the TOR of propylene oxide on the largest particles (23.3 nm) at 200 °C.

The surface-atom based TORs show an interesting, non-linear decrease of activity with increasing size and corresponding surface area and volume. Considering the two smallest Ag clusters (average lateral diameters #3 = 8.7 nm and #2 = 12 nm), the surface-atom based TOR for PO decreases by about only 10% while acrolein production drops by about 90% with the slightly increased cluster size. For the largest Ag cluster (average lateral diameter #1 = 23.3 nm), the surface-atom based TORs drop by about a factor of 10 for both propylene oxide and acrolein. Thus, as we found above for the TOR's as a function of temperature, the reaction specificity also suggests that the mechanism for the catalytic reaction is significantly different for the larger clusters. We note that the smaller clusters have a much higher structural fluxionality, than their larger cousin.

The observed high TOR for propylene oxide formation at 200 °C on the ~9 nm particles reported here is only about ~30% lower than that observed for 2 nm tall and 4 nm in diameter silver particles made by aggregation of size-selected sub-nanometer silver trimer clusters [25], thus potentially indicating a new, sub-10 nm size range for highly active silver-based alkene partial oxidation catalysts. In comparison with reported silver-based propylene

**Table 1**
Turn-over rates of propylene oxide and acrolein formed at 200 °C per total and exposed silver surface atom basis.

| Cluster sample | Ag cluster mean lateral diameter (nm) | TOR of propylene oxide produced | | TOR of acrolein produced | |
|---|---|---|---|---|---|
| | | [PO molecules × total Ag atoms$^{-1}$ s$^{-1}$] | [PO molecules × exposed surface Ag atoms$^{-1}$ s$^{-1}$] | [Acr molecules × total Ag atoms$^{-1}$ s$^{-1}$] | [Acr molecules × exposed surface Ag atoms$^{-1}$ s$^{-1}$] |
| #1 | 23.3 | $3.7 \times 10^{-3}$ | $8.5 \times 10^{-2}$ | $2.0 \times 10^{-3}$ | $4.8 \times 10^{-2}$ |
| #2 | 12.0 | $7.2 \times 10^{-2}$ | $8.9 \times 10^{-1}$ | $7.9 \times 10^{-2}$ | $5.2 \times 10^{-1}$ |
| #3 | 8.7 | $1.2 \times 10^{-1}$ | 1.1 | $5.0 \times 10^{-1}$ | 4.3 |

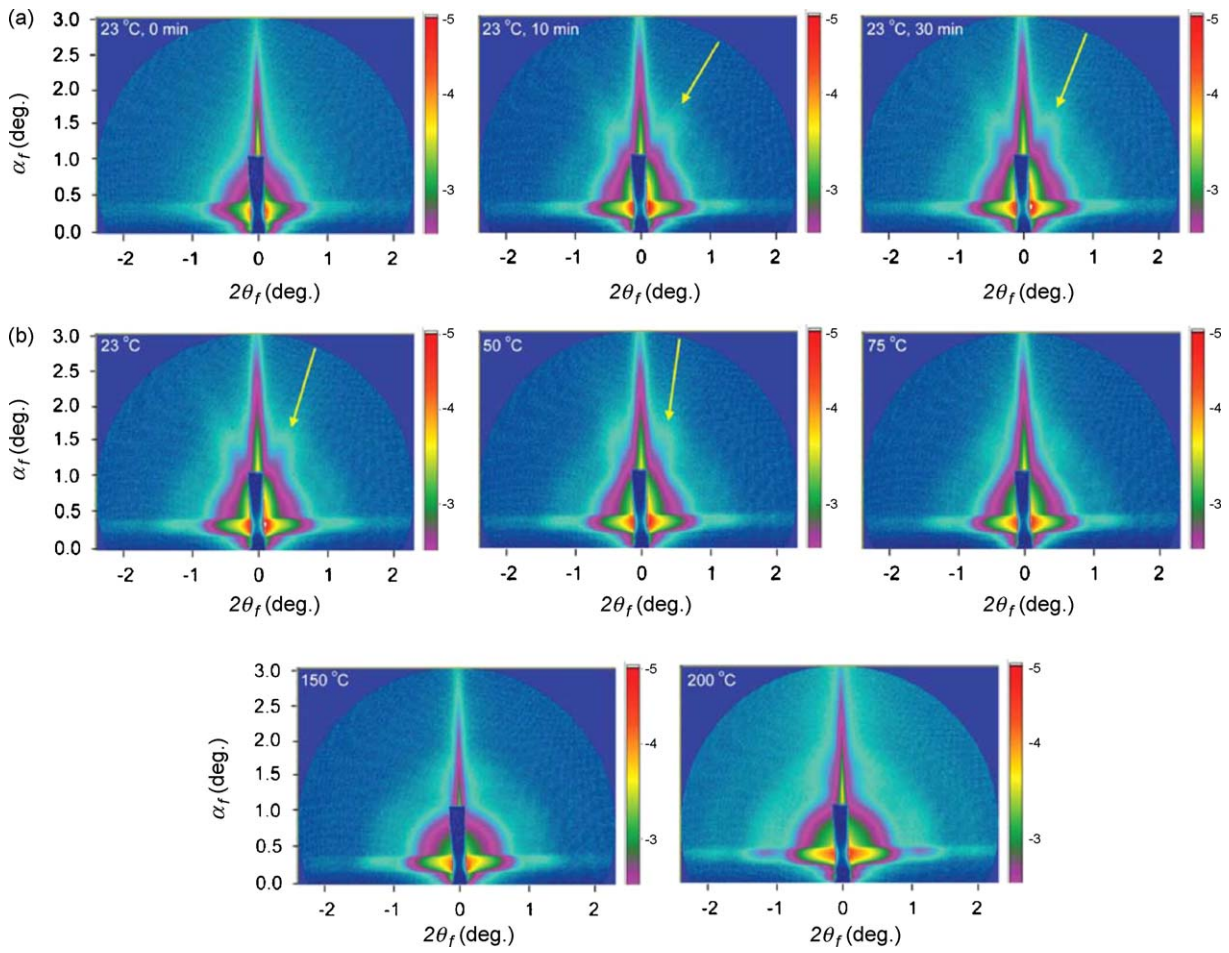


**Fig. 8.** GISAXS images on ~9 nm large particles. (a) At room temperature, from left to the right: image recorded at the time of the inlet of the propylene–oxygen mixture, after 10 min of exposure and after 30 min of exposure. (b) Change of the scattering pattern during ramping the temperature from 23 to 200 °C. The arrows indicate the angle of the most intense component of the directional scattering.

epoxidation catalysts, the TOR for the 9 nm sized clusters per surface atom or per atom is high. For instance, the rate of propylene oxide molecule formation per surface silver atom is about 1.1 $s^{-1}$ at 200 °C for the 9 nm particles, which is much greater than that reported for larger silver particles. For example, turn-over rates per surface atom ($\leq 10^{-4}$ per total atom) is reported to be $1 \times 10^{-2}$ $s^{-1}$ for 50–660 nm unpromoted silver particles at 220 °C [5] and about $5 \times 10^{-3}$ $s^{-1}$ for a 3:1 weight ratio Ag/Ni catalyst tested in the 150–300 °C temperature range [94]. Thus, the turn-over rates in this work are more than an order of magnitude higher than the previously reported data by other groups (for reference data see Supplemental Online Material of reference [25] for TORs on either a per surface atom or a per atom basis).

The propylene oxide to acrolein ratio at 200 °C is plotted in Fig. 7, showing a change in selectivity by over an order of magnitude in the cluster size range ~9 to ~23 nm, reinforcing the conclusions drawn from Table 1. It is noteworthy that acrolein formation occurs at lower temperature than the temperature for propylene oxide formation, and no onset temperature could be found for this reaction, indicating that acrolein formation has a very low activation barrier and that surface oxygen may be involved in the production of acrolein, rather than subsurface oxygen whose formation requires higher temperatures [1,2,91,95]. Particle size-dependent oxidation properties have been reported by Bukhtiyarov and Kaichev [91] in the epoxidation of ethylene. Their results show that concentration of oxygen in silver catalysts is particle size dependent, and reactive (subsurface) oxygen appeared for particle sizes greater than 30 nm, which was associated with the rate of epoxidation of ethylene. Also it has been reported that adsorbed molecular oxygen is responsible for the formation of acrolein, whose formation is favoured on isolated silver sites [1].

As shown in Fig. 7, there is a pronounced effect of particle size on the selectivity. The smaller size silver clusters may stabilize adsorbed molecular oxygen more efficiently than the bigger clusters, on which $O_2$ dissociatively adsorbs to form subsurface oxygen preferentially. Surface oxide structure of silver has been in long debate [54,55,96–99] and high pressure subsurface oxide formation is not clearly understood [100]. Our results may indicate that, under given reaction conditions of steady state oxygen concentration, the silver oxide formation and equilibrium between surface and subsurface oxygen is particle size dependent, which can represent a key factor in controlling the selectivity in the oxidation of propylene. No change in the mass signal corresponding to carbon dioxide is observed during the temperature ramp. Presumably, low oxygen to propylene ratio (1:2) of the reaction gas effectively suppresses total oxidation.

### *4.3. In situ GISAXS and HRETEM: change in faceting of the particles*

Fig. 8 shows a sequence of *in situ* GISAXS images of ~9 nm large silver particles recorded during the oxidation of propylene. Fig. 8a shows the change in scattering pattern at room temperature caused by the reactants. Few minutes after the inlet of the

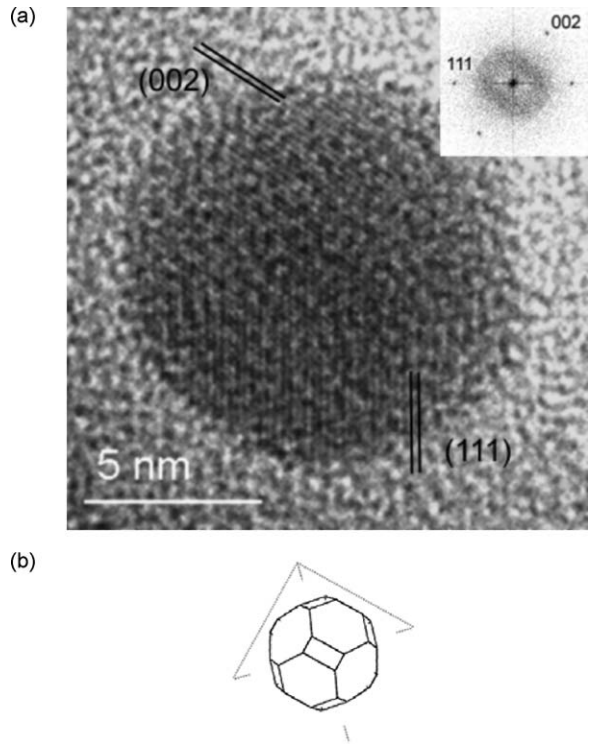


**Fig. 9.** (a) HRETEM of silver cluster under hydrogen. (b) Wulff shape reconstruction.

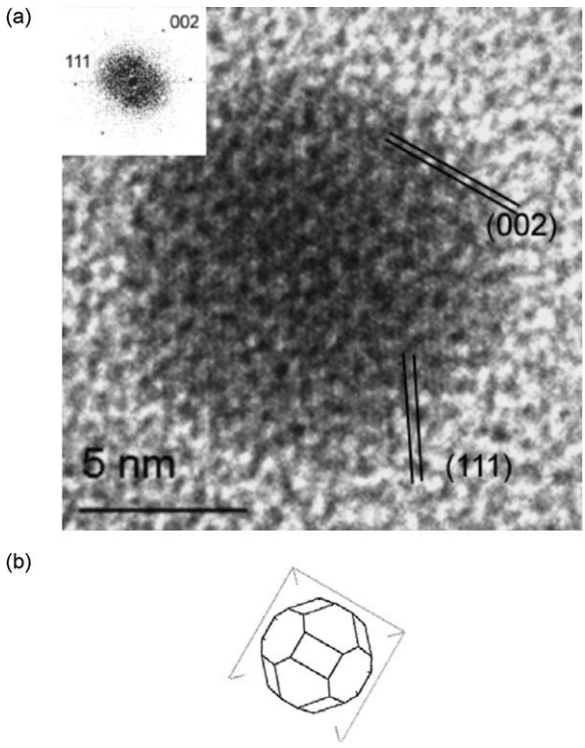


**Fig. 10.** (a) HRETEM of silver cluster under oxygen. (b) Wulff shape reconstruction.

reactants a directional scattering emerges (indicated by arrows), with its angle changing with time. As discussed below, we ascribe this to the growth of (1 1 1) facets—a reshaping accompanied by the reorientation of the particles. Fig. 8b shows the further evolution of the scattering pattern with temperature as the reaction proceeds. The directional scattering vanishes above 75 °C and the symmetrical scattering pattern at 200 °C is indicative of the formation of spherical particles at this temperature. Such directional scattering is observed for example on much larger palladium and silver nanoparticles [45,72].

In order to unambiguously attribute the observed pattern to facets, we have imaged silver nanoparticles in environmental HR TEM (HRETEM) under oxygen and hydrogen. Hydrogen was chosen instead of propylene to mimic competition for oxygen binding with propylene on the surface of the particles in order to avoid possible contamination of the environmental TEM cell.

The results are shown in Fig. 9 and reveal faceted particles. A reversible change in faceting structure is observed when alternating between oxygen and hydrogen environment. Fig. 9a shows a silver cluster under $H_2$ at a pressure of $3.95 \times 10^{-3}$ atm. According to the high-resolution images and their calculated Fast Fourier-Transforms, the cluster is (1 1 0) oriented. In such an orientation, the lateral faces parallel to the electron beam are (0 0 2) and (1 1 1) faces.

The shape is limited by extended (1 0 0) and (1 1 1) surfaces, and by (1 1 0) small surfaces. The Wulff shape fitting to the external shape is represented in Fig. 9b. The series of Wulff shapes of an fcc cluster in the same (1 1 0) orientation were simulated for varying ratios between the surface free energies $\sigma_{111}$, $\sigma_{001}$ and $\sigma_{110}$. The $\sigma$ values were used with increasing steps of 0.1 J m$^{-2}$, from 0.9 to 1.3 J m$^{-2}$ (see for example Ref. [101]). The comparison between the calculated shapes and experimental ones allows the estimation of the ratios $\sigma_{001}/\sigma_{111}$, and $\sigma_{110}/\sigma_{111}$. According to this shape, the central distances to the limiting (1 0 0), (1 1 1) and (1 1 0) facets are evaluated. According to the Wulff theorem, $h_i/h_j = \sigma i/\sigma j$, their ratio corresponds to the ratio between the surface free energies $\sigma_{100}$, $\sigma_{111}$ and $\sigma_{110}$. The values of the anisotropy ratios are yield $\sigma_{100}/\sigma_{111} = 1.00$ and $\sigma_{110}/\sigma_{111} = 1.11$.

Fig. 10a shows the HRETEM image of the same silver cluster in pure $O_2$ at the same pressure after a few minutes. The cluster is still (1 1 0) oriented but the shape limited by (1 0 0), (1 1 1) and (1 1 0) faces is more isotropic. The Wulff shape fitting to the external shape observed in $O_2$ is represented in Fig. 10b. In this case, the values of the anisotropy ratios are evaluated to $\sigma_{100}/\sigma_{111} = 1.00$ and $\sigma_{110}/\sigma_{111} = 1.055$.

The effect of pure oxygen has previously been observed by the same technique on Au clusters of the same size, supported on carbon [67] or $TiO_2$ [102]. At variance with what was observed for Ag clusters, the effect of pure $O_2$ on Pt clusters on carbon [103] and Pd clusters supported on MgO [66], induces an extension of the (0 0 1) faces at the expense of the (1 1 1) faces. In the case of small Pd and Au clusters [104], the experimental values from HRETEM observations in vacuum were also found to have extended the (0 0 1) facets ($\sigma_{100}/\sigma_{111} = 1.15$). The electron beam effect on the morphology of the particles has been studied for example in Ref. [105].

In the case of the Ag clusters, the variations of the anisotropy ratio between the (1 0 0) and (1 1 1) facets in $H_2$ and $O_2$ at a pressure of $4 \times 10^{-1}$ kPa, at room temperature were very small. On the opposite side, the more open faces (1 1 0) are extended with $O_2$ exposure. The HRETEM results provided very important proof about the existence of facets and their alteration caused by changes in the gas composition at lower temperatures, as indicated by GISAXS. However, due to differences between the gas composition and pressure in the GISAXS and HRETEM experiments, as well as the different composition of the support used, a direct quantitative comparison between both experiments would be difficult.

Fig. 11 shows a representative GISAXS image with facet scatterings from ~9 nm large nanoparticles. The blue solid arrows denote all possible contributions from (1 1 1) facet scatterings from a single crystalline nanoparticle oriented in a way that their (2 1 1) plane is parallel to the substrate surface but randomly oriented in the sample plane. The black dotted arrows indicate the possible con-

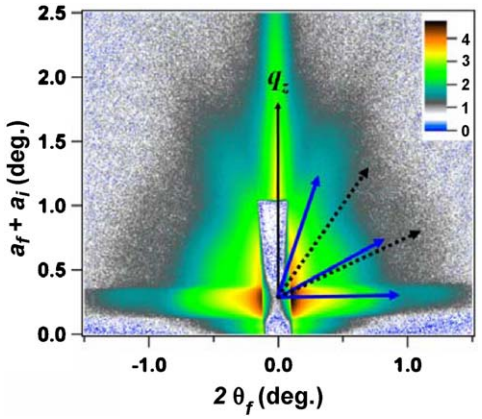


**Fig. 11.** Analysis of the GISAXS pattern of a ~9 nm large silver particles when exposed to the mixture of propylene and oxygen. The arrows indicate scattering from various facets. The blue solid arrows denote possible contributions from (1 1 1) facet scattering from single crystalline nanoparticles. The black dotted arrows denote the possible contributions from (1 1 0) facet scatterings from the same particles. Note that arrows are shown only on the right half of the image, since the GISAXS pattern is symmetrical with respect to the $q_z$ axis.

tributions from (1 1 0) facet scatterings from the same particles. The azimuthal angles (the angle between $q_z$ and facet scattering) of (1 1 1) facet scattering are 19.5°, 61.9°, and 90° [106]. Facet scatterings in the measured GISAXS images are well matched with the calculated (1 1 1) facet direction shown by arrows suggesting that (1 1 1) plane is a dominant facet of Ag nanoparticles under the mixture of propylene and oxygen. The disappearance of the directional scattering at higher temperatures (cf. Fig. 8) demonstrates the loss of (1 1 1) faceting and may be indicative of changes of the surface energies in the presence of catalytic reactions leading to more spherical particle shapes and/or the formation of disordered surface structures.

## 5. Results of theoretical calculations and discussion

### 5.1. Oxygen adsorption

The Ag particles as deposited are left in air for several days. Under these conditions, $O_2$ molecules dissociate over silver surfaces, and some degree of surface oxidation can be assumed. We argue that at room temperature and atmospheric pressure the exposure of the silver clusters to oxygen produces only chemisorbed species. Under mild conditions, in fact, the energy barriers for complex surface reconstructions leading to the formation of subsurface oxygen species are too high to overcome. This assumption is supported by experiment, which shows that oxygen-induced reconstructions of compact surfaces are formed only above at least 100 °C [107] or in the presence of defects [93]. We focus on the adsorption of oxygen atoms over the most compact metal surfaces, namely the (1 1 1), (1 0 0) and (1 1 0) ones (which are those experimentally observed by HRETEM) and at low coverages (up to 0.5 ML). At higher coverages, the occupation of subsurface sites becomes favoured [97,108].

Detailed studies of the oxygen adsorption process on the (1 0 0) and (1 1 1) surfaces have been already carried out in the literature [97,108]. Our calculations on these surfaces aim at validating our approach and for assuring consistency with the calculation performed on the (1 1 0) surface.

We evaluate the adsorption energy ($\Delta E_{ads}$) of an oxygen atom according to the relation [108]:

$$\Delta E_{ads} = \frac{1}{N_o}\left[E_{tot} - E_{Ag} - \frac{N_o}{2}E_{O_2}\right]$$

where $E_{tot}$ is the total energy of the composite system, $E_{Ag}$ is the energy of the clean silver surface, $E_{O_2}$ is the energy of an oxygen molecule and $N_o$ is the number of oxygen atoms adsorbed on the surface. Recall that our DF/PBE approach overestimates the binding energy of the oxygen molecule (6.6 eV against the experimental value of 5.1 eV), and we expect that the oxygen/silver interaction is similarly overestimated, as suggested by comparison with experiment on strongly oxidized surfaces [54,55] . To evaluate the Gibbs free energy corresponding to the adsorption process ($\Delta G_{ads}$), the $O_2$ molar Gibbs free energy is calculated in the perfect gas approximation, e.g., 0.54 eV at room temperature (298 K) and standard pressure (1 atm). Both $\Delta E_{ads}$ and $\Delta G_{ads}$ are reported in Table 2 for selected cases.

#### 5.1.1. Oxygen adsorption on Ag (1 0 0) surface

In the case of the (1 0 0) surface, the most favourable adsorption site for oxygen is a four-fold hollow position. In this site, oxygen is surrounded by eight metal atoms (four in-plane and four below the surface). Looking at the results reported in Table 2, we can see that the adsorption energy is not appreciably modified in passing from 1/9 to 1/4 coverage, but is reduced from 0.70 to 0.57 eV due to the Coulombic repulsion between the negatively charged adatoms when the concentration is increased to 1/2 (and the atoms are arranged according to a $c(2\times2)$ pattern (see Fig. 12a) At higher coverage, configurations involving the occupation of subsurface sites become energetically favoured with respect to simple chemisorption. The values of $\Delta G_{ads}$ are negative, implying that the adsorption process occurs spontaneously. From Table 2 a coverage of 1/2, characterized by a $c(2\times2)$ arrangement of the adatoms (Fig. 12a), results as a good estimate of the real coverage of the (1 0 0) surface.

#### 5.1.2. Oxygen adsorption on Ag (1 1 1) surface

On the (1 1 1) surface, which has also been the subject of previous studies (e.g. [97,109]), the most favourable adsorption sites for oxygen atoms are three-fold hollow sites. In these sites the interac-

**Table 2**
Adsorption energies ($\Delta E_{ads}$) and Gibbs free energies ($\Delta G_{ads}$) related to oxygen adsorption on the lowest-energy silver surfaces. The coverage is defined by the ratio between the number of adatoms and the number of surface hollow sites.

| Surface | Coverage | Unit cell | # of adatoms | $\Delta E_{ads}$ (eV) | $\Delta G_{ads}$ (eV) | Figure |
|---|---|---|---|---|---|---|
| (1 0 0) | 1/9 | (3 × 3) | 1 | 0.71 | 0.44 | |
| | 1/4 | (2 × 2) | 1 | 0.70 | 0.43 | |
| | 1/2 | (2 × 2) | 2 | 0.57 | 0.30 | Fig. 12a |
| (1 1 1) | 1/9 | (3 × 3) | 1 | 0.38 | 0.11 | |
| | 1/4 | (2 × 2) | 1 | 0.35 | 0.08 | |
| | 1/2 | (2 × 2) | 2 | ~0 | <0 | Fig. 12b |
| (1 1 0) | 1/9 | (3 × 3) | 1 | 0.45 | 0.18 | |
| | 1/4 | (2 × 2) | 1 | 0.42 | 0.15 | |
| | 1/2 checkboard | (2 × 2) | 2 | 0.30 | 0.03 | Fig. 12c |
| | 1/2 [1 1 0]-row | (2 × 2) | 2 | 0.41 | 0.14 | Fig. 12d |
| | 1/2 [1 1 1]-row | (2 × 2) | 2 | 0.08 | <0 | |

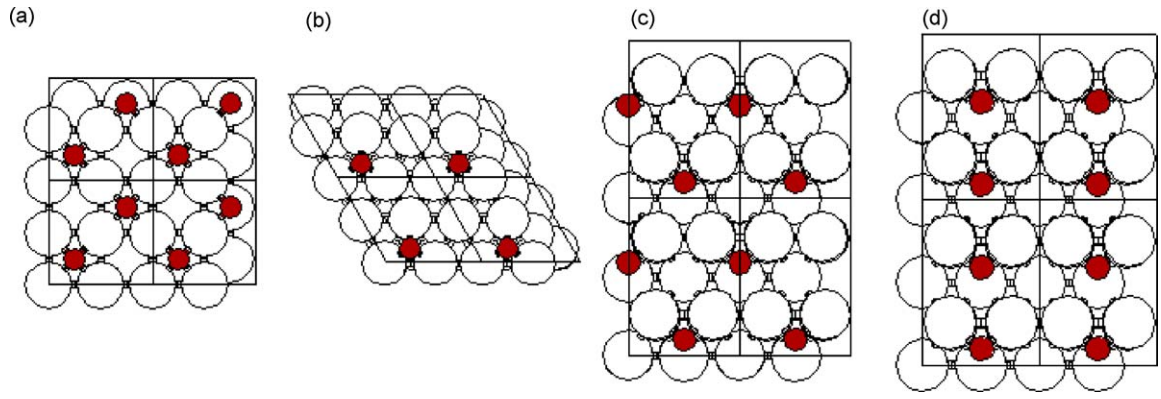


**Fig. 12.** Oxygen adatoms on the (a) (1 0 0) surface according to a 1/2 coverage and a $c(2 \times 2)$ pattern; (b) (1 1 1) surface according to a 1/4 coverage and a $p(2 \times 2)$ pattern; (c) (1 1 0) according to a 1/2 coverage and a $c(2 \times 2)$ pattern; (d) (1 1 0) surface according to a 1/2 coverage and a [1 1 0]-row pattern. Silver atoms are displayed in white, oxygen atoms in red. Four unit cells are displayed in each case.

tion with the surface is decreased with respect to the (1 0 0) surface, as metal atoms have higher coordination and the number of Ag–O bonds is smaller. Looking at the numbers of Table 2, we can see that at coverage of 1/9 and 1/4 on the (1 1 1) surface the interaction energy is decreased by a factor of 2 with respect to the case of the (1 0 0) surface (for example, 0.35 eV instead of 0.70 eV at 1/4), whereas at a coverage of 1/2 the adsorption process results energetically unfavourable. The values of the corresponding Gibbs free energies are consequently reduced with respect to the (1 0 0) surface, so that adsorption is spontaneous only up to a coverage of 1/4 (this structure is shown in Fig. 12b). This implies also that the density of oxygen adatoms on the (1 1 1) surface is decreased with respect the (1 0 0) case.

#### 5.1.3. Oxygen adsorption on Ag (1 1 0) surface

The (1 1 0) surface exhibits an intermediate behavior between the previous two cases. The most favourable adsorption sites are the three-fold hollow sites, as in the (1 1 1) surface, but the metal coordination of the three first-neighbour atoms is reduced, so that the adsorption energy is a bit higher than on the (1 1 1) surface (0.42 eV instead of 0.35 eV at 1/4, see Table 2) and is only slightly decreased in passing from 1/9 to 1/4 coverage. In Fig. 12c and d we show two possibilities of adsorption at coverage of 1/2 among the several cases investigated. The checkboard pattern (Fig. 12c) is similar to the $c(2 \times 2)$ arrangement of the (1 0 0) surface and corresponds to a drastic reduction of the adsorption energy with respect to lower coverage. A better arrangement is realized in the configuration shown in Fig. 12d, in which the oxygen atoms are organized in rows running along the [1 1 0] direction. The same row pattern along the [1 1 1] direction (rows perpendicular to the former ones) is disfavoured, as the adsorption energy is only 0.08 eV per adatom. The 1/2 coverage in the [1 1 0]-row arrangement is thus a reasonable model for the oxygen adsorption on this surface.

### 5.2. Cluster reshaping

In Table 3, we report the values of surface energy for the (1 1 1), (1 0 0) and (1 1 0) surfaces when they are clean and in case of oxygen adsorption at room temperature and $p(O_2) = 1$ atm and $p(O_2) = 5 \times 10^{-3}$ atm, respectively, as evaluated using our DF/PBE energy values. In the presence of oxygen adsorption, the surface energies are decreased, due to stabilization via oxidation. This stabilization is strongest in the case of the (1 0 0) surface, characterized by the largest interaction with the oxygen atoms and by a high density of adatoms: the surface energy is decreased from 801 to 525 mJ/m$^2$ at $p(O_2) = 1$ atm. On the contrary, the (1 1 1) surface is the one experiencing the smallest energy gain: its surface energy changes from 742 to 700 mJ/m$^2$ at $p(O_2) = 1$ atm, due to the weaker interaction with oxygen atoms and to the lower density of adatoms. It should be recalled however, as noted above, that our DF/PBE approach probably overestimates the ratio of Ag–O vs Ag–Ag binding energies, and correspondingly the stabilization of (1 0 0) vs (1 1 1) surface.

Such changes in surface energies are reflected in a reshaping of the supported silver clusters in the absence or presence of oxygen. We apply the Wulff–Kaishev construction to derive the equilibrium shape of the supported metallic particles. In Fig. 13, we show the equilibrium shape of representative supported silver particles in the case of clean surfaces (Fig. 13a) and in the case of oxygen adsorption at $p(O_2) = 1$ atm (Fig. 13c) and at $p(O_2) = 5 \times 10^{-3}$ atm (Fig. 13b). For simplicity, we take into account only (1 1 1) and (1 0 0) surfaces. Furthermore, we assume a (1 1 1) epitaxy with an adhesion energy equal to 0.20 eV per interacting atom (a reasonable estimate for a simple ionic oxide, see e.g. Ref. [110]. The interaction with the substrate translates into a further energy gain for the surface in contact with the support, and as a consequence an increase of the contact area with respect to the opposite face. For clean particles, the anisotropy ratio between the energy of the (1 0 0) and (1 1 1) surfaces is 1.08, entailing that the area of the (1 1 1) faces

**Table 3**
Energies of the (1 1 1), (1 0 0) and (1 1 0) silver surfaces in the case of clean surface and in the presence of oxygen adatoms at $p(O_2) = 1$ atm and $p(O_2) = 5 \times 10^{-3}$ atm. In the table, the equilibrium oxygen coverage is also reported, with the corresponding Gibbs free energy per oxygen adatom.

| | Surface | (1 1 1) | (1 0 0) | (1 1 0) |
|---|---|---|---|---|
| $p(O_2) = 0$ atm | Clean surface (mJ/m$^2$) | 742 | 801 | 891 |
| | Oxygen coverage | 1/4 | 1/2 | 1/2 |
| | $\Delta G_{ads}$ (eV) | 0.08 | 0.30 | 0.14 |
| $p(O_2) = 1$ atm | Energy gain (mJ/m$^2$) | 42 | 276 | 91 |
| | Covered surface (mJ/m$^2$) | 700 | 525 | 800 |
| | $\Delta G_{ads}$ (eV) | – | 0.23 | 0.07 |
| $p(O_2) = 5 \times 10^{-3}$ atm | Energy gain (mJ/m$^2$) | – | 211 | 46 |
| | Covered surface (mJ/m$^2$) | 742 | 590 | 845 |

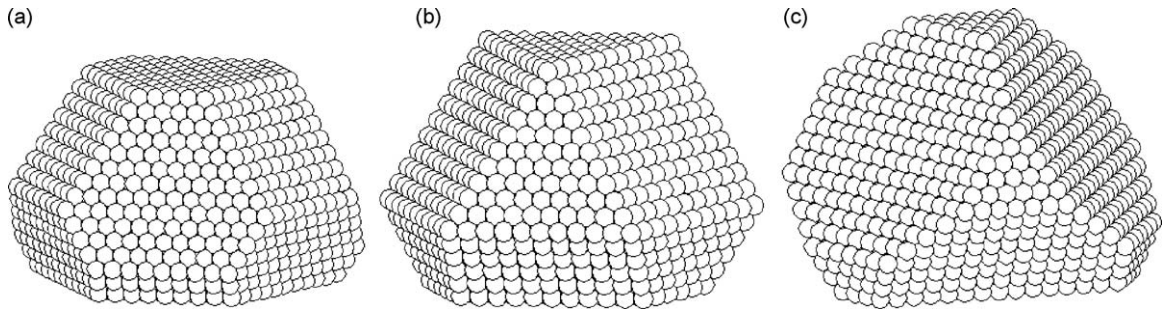


**Fig. 13.** Morphology of supported silver particles in case of (a) non-oxidized surfaces, and oxygen-covered surfaces at (b) $p(O_2) = 5 \times 10^{-3}$ atm and (c) $p(O_2) = 1$ atm. The lateral dimension of the clusters is about 6 nm.

is larger than that of the (1 0 0) faces—see Fig. 13a. In contrast, in the presence of oxygen adatoms, the ratio is decreased to 0.80 at $p(O_2) = 5 \times 10^{-3}$ atm or to 0.75 at $p(O_2) = 1$ atm, entailing an increase in the area of the (1 0 0) faces—see Fig. 13b and c. The calculated aspect ratio of the cluster, i.e., the ratio between the lateral dimension and the height of the cluster is 1.75 in the absence of oxygen adsorption, whereas it becomes 1.44 and 1.53 at $p(O_2) = 1$ atm and $p(O_2) = 5 \times 10^{-3}$ atm, respectively.

If we assume that propylene in the absence of oxygen produces a removal of oxygen atoms from the surface and thus a morphology change to the gas-phase shape of the particles, our predicted aspect ratio is 1.75 for the clean particles. The predicted aspect ratio of 1.53 for the oxidized particles at $p(O_2) = 5 \times 10^{-3}$ atm is somewhat smaller than the experimentally determined ~1.6 aspect ratio of the oxidized silver particles in the absence of propylene (but see the warning above). When propylene and oxygen are co-fed in the reaction mixture, a steady state will be reached, which will depend on the flux, the propylene/oxygen ratio, etc., and in which the oxidation state of the particles' surfaces will probably be intermediate between the two limit conditions (pure propylene and pure oxygen).

The situation is much more complex at $T > 100\,^{\circ}C$. In such conditions, in fact, formation of complex surface reconstructions is thermodynamically and kinetically favoured, on both the (1 0 0) [111] and the (1 1 1) [55,56,106] surfaces. However the formation of a thick shell of silver oxide is excluded by HRETEM and GISAXS data as well as XPS on ~3.5 nm size silver aggregates [25]. In particular, XPS data set an upper limit of ~5% to the oxygen content of the surface on small nanoparticles [25]. This is compatible with the formation of oxidized surface layers, but not with a thick AgO shell. Formation of structurally complex surface reconstructions in which a mixture of different phase is realized are discussed in Refs. [55,56,97,107,111] and is also consistent with the experimental observation at GISAXS that the particles lose faceting at higher temperatures (c.f. Fig. 8).

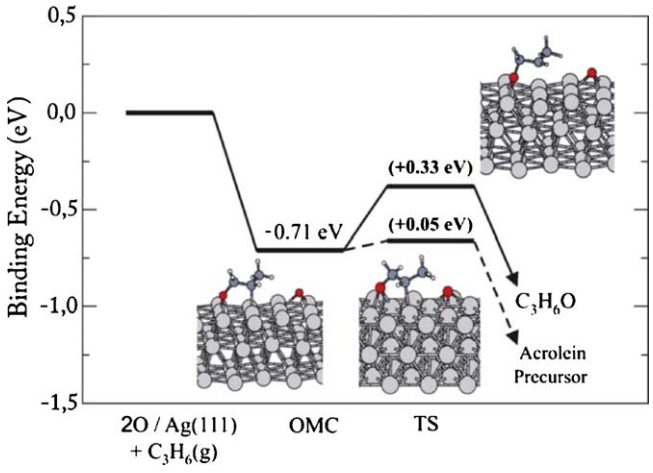


**Fig. 14.** Structures (see insets) and binding energies for the reaction of propylene with oxygen adatoms at the Ag(1 1 1) surface. The filled and dashed lines represent the pathways for propylene oxide or acrolein formation, respectively. In bold and parenthesis, values for the activation barriers. OMC and TS represent, respectively, the reaction steps involving propene oxametallacycle formation and the Transition State for either acrolein or propene oxide formation. Upper inset shows TS for $C_3H_6O$ formation; lower inset to the right the TS for acrolein formation (involving hydrogen transfer from propene methyl group to oxygen surface adatoms). Red, white, dark gray and light gray spheres represent, respectively, O, H, C and Ag atoms. We take as reference energy (0.0 eV) the energy of gas-phase propene and of two oxygen adatoms on the Ag(1 1 1) surface.

## 5.3. Catalysis

### 5.3.1. Interaction of propylene or propylene/oxygen mixture with Ag particle surface

In order to gain a better understanding of the experimental results under catalytic conditions, the interaction of propylene with various models of oxygen-covered silver nanoparticles have been studied, considering cases with both small and large concentrations of surface oxygen (in the latter case, leading to the effective formation of a thin surface oxide). In the first place, we use the Ag(1 1 1) surface as a reasonable approximation of facet sites on large (~10 nm) nanoparticles. Two oxygen adatoms are then placed on the surface, and pathways for either propylene oxide ($C_3H_6O$) or acrolein ($C_3H_4O$) formation are evaluated, starting from a propylene oxametallacycle (OMC) intermediate. The

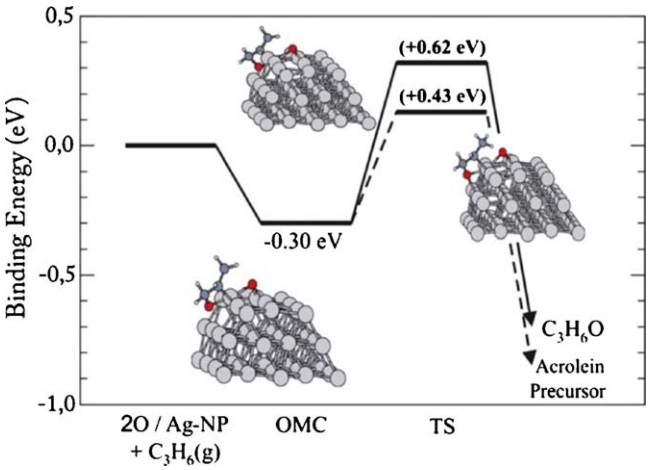


**Fig. 15.** Structures (see insets) and binding energies for the reaction of propylene with oxygen adatoms at a model of the edge sites in a Ag nanoparticle. Same convention as in Fig. 14. The upper inset represents the Transition State for propylene oxide formation, whereas the inset to the right represents the TS for acrolein formation. The lower inset to the left shows the equilibrium structure of the adsorbed propene oxametallacycle (OMC). Values for reaction barriers are shows as bold and in parenthesis.

results in Fig. 14 show a relatively high stability (0.7 eV) of the propylene OMC intermediate; this fact can be understood in terms of a quite high reactivity of the supported oxygen adatoms. This value is somewhat larger than the ones found for the analogous ethene OMC on Ag(1 1 1), which has been extensively studied in the past [52,107,112–115], being of the order of 0.4 eV. Then, starting from the OMC intermediate, we have calculated the energy barriers for the competitive steps of either closing the cycle (propylene oxide formation) or hydrogen transfer from the propylene methyl group towards a neigbouring oxygen adatom, which represents the first step of acrolein formation. We find a sizable barrier of 0.33 eV for the formation of propylene oxide, much higher than the one for hydrogen transfer, which is almost a barrierless process (only 0.05 eV barrier). Similar results were found for the (1 0 0) and (1 1 0) surfaces. We can therefore conclude that, at low oxygen coverage, facet sites will be more selective towards acrolein production than towards propylene oxide formation.

### 5.3.2. Interaction of propylene or propylene/oxygen mixture at Ag particle edges

In the case of nanoparticle edge sites, the situation is somewhat changed. To obtain a relatively accurate model of this type of sites, at a reasonable computational cost, we employed a one-dimensional silver rod, which takes advantage of the periodic symmetry requirements introduced by our plane-wave-based DF approach. The insets in Fig. 15 show perspective views of the unit cell for the relaxed rod structure, 4 Ag atoms long (a size that we estimate large enough to minimize intercell interaction). Then, dissociation of $O_2$ at the edge leads to a configuration with two oxygen adatoms placed at both sites of the silver edge (several conformations of the two oxygen adatoms were tested, in order to find the most stable structure).

The higher reactivity of these sites causes chemisorbed oxygen atoms to bind more strongly to silver, with a binding energy (with respect to gas-phase $O_2$) of 0.73 eV (the binding energy at Ag(1 1 1) is only 0.31 eV). Then, we have again analyzed the propylene interaction with the slightly oxidized model catalyst. The results in Fig. 15 show a weaker propylene OMC–silver interaction (0.30 eV formation energy); this is due to the stronger binding of oxygen to silver at these more reactive sites, which causes in turn a weakening of the C–O bond strengths. Then, starting from the OMC intermediate, we have calculated the energy barriers for either propylene oxide or acrolein formation (again, by hydrogen transfer from the propylene methyl $-CH_3$ group to the second oxygen adatom). In both cases, the barriers rise (with respect to the Ag(1 1 1), i.e., facet sites case), and, although selectivity towards acrolein is larger, the difference in barrier height is now much reduced.

### 5.3.3. Interactions of propylene or propylene/oxygen mixture with Ag particle surface: high oxygen coverage

We now move to the case of high oxygen coverages (which can induce formation of a thin surface oxide). As a model of the highly oxidized silver Ag(1 1 1) surface (presumably, with a similar structure to the one of the facets of relatively large silver nanoparticles), we take the $Ag_{1.83}O$/Ag(1 1 1) thin silver oxide found in STM-UHV experiments by Bocquet et al. [107]. This structure has been also identified through DF simulations as particularly stable by Li et al. [97], being likely to form at temperatures above 100 °C. Fig. 16a shows the side and top view of the p(4 × 4) unit cell; the surface oxide structure is based on a honeycomb-like lattice of alternating O–Ag–O bonds, where half of the oxygen atoms are placed on top of the first Ag layer and another half below it. Next, half of the hexagons are filled by Ag atoms placed in their centers. In agreement with DF simulations by Bocquet and Loffreda [112], we find a 0.15 eV binding energy of "intact" propylene (i.e., with a double C=C bond) to the oxide, bonded to a Ag atom. Formation of

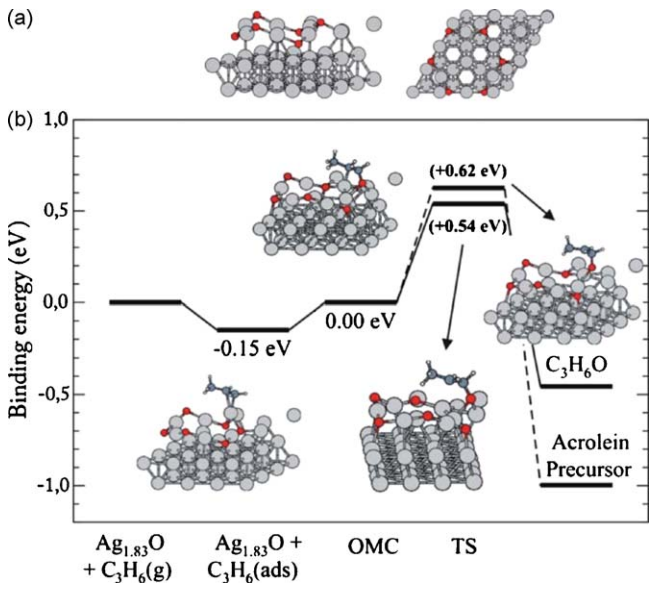


**Fig. 16.** (a) Top and side views of the model for the oxidized silver surface, being a $p(4 \times 4)$ unit cell of the $Ag_{1.83}O$/Ag(1 1 1) surface oxide. (b) Structures (see insets) and binding energies for the reaction of propylene with the oxidized Ag(1 1 1) surface. The first reaction step ($C_3H_6$ adsorption) is included. Same atom coloring as in Fig. 14. We take as energy reference (0.0 eV) the energy of gas-phase propene plus the energy of the oxidized silver surface. The two insets to the right show the structures of the Transition States for either acrolein (dashed line) or propylene oxide (full line) formation. The lower inset to the left shows the structure for propene adsorption, whereas the upper left inset shows the relaxed structure for the propene oxametallacycle (OMC). Values for energy barriers shown in bold and between parentheses.

the propylene OMC intermediate is thermoneutral, with a 0.0 eV binding energy (with respect to gas-phase propylene), which indicates a much less reactive character of the oxygen atoms which are now part of the surface oxide. All these facts indicate a relatively inert character of the surface, which agrees well with the experimentally observed low reactivity of the larger Ag nanoparticles. As for the selectivity, we find a completely different behavior with respect to the low oxygen coverage situation; now the energy barrier towards acrolein production is actually higher (0.62 eV) than the one for propylene oxide production (0.54 eV). We interpret this finding in terms of the absence of reactive oxygen species in the vicinity of the OMC intermediate, caused by the special structure of the surface oxide. The only oxygen atom available for oxygen transfer lies actually subsurface, and it costs a sizable amount of energy to drive it upwards towards the propylene OMC methyl group. In addition, we have also checked other reaction pathways involving direct reaction between the methyl group of "intact" adsorbed propylene (inset to the right in Fig. 16b) and neighboring oxygen atoms, but they turned out to be unfeasible due to the lack of a C–O covalent bond (present in the OMC case) which helps on stabilizing the final state.

### 5.3.4. Interactions of propylene or propylene/oxygen mixture at Ag particle edges: high oxygen coverage

Finally, we have considered the case of nanoparticle edge sites at high oxygen coverage; we employ again the one-dimensional rod model system, saturating one of its edges with adsorbed oxygen atoms. The results are shown in Fig. 17. We find that, after fully relaxing the model system, very important surface reconstructions occur, although the local chemical features at the edge atoms are not qualitatively changed; as in the case of low coverage, two oxygen atoms are placed at each of the sides of the Ag edge atoms. Interestingly, the overall features of the edge reactivity and selectivity do not strongly change with respect to the

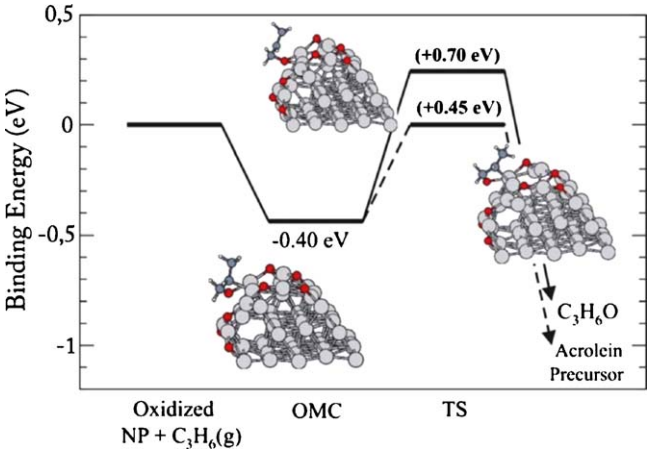


**Fig. 17.** Structures (see insets) and binding energies for the reaction of propylene with a model of oxidized nanoparticle edge sites. Same atom coloring as in Fig. 14. Dashed and full lines represent, respectively, pathways for acrolein or propylene oxide formation. The inset to the right shows the Transition State for acrolein formation, and the upper inset the TS for propene oxide formation. The lower inset to the left shows the relaxed structure for the propylene oxametallacycle (OMC). Values for energy barriers are shown in bold and between parentheses.

low coverage case, with a similar propylene OMC stability, and a preference towards acrolein formation (with, actually, a larger difference between the values of the barriers). Comparing this situation with the $Ag_{1.83}O$/Ag(1 1 1) case, the most striking difference (which causes the selectivity towards acrolein to drastically change) is the availability of exposed reactive oxygen adatoms in the vicinity of the propylene OMC. This fact is caused, as it can be seen in the relaxed structures, by the special topology and irregularities introduced by the presence of such defect-like edge sites.

*5.3.5. Discussion of the theoretical results*

Overall, the results from the DF simulations agree with the behavior observed in the experiments. At low temperature, where the oxygen coverage is relatively low, and surface oxides do not form, propylene oxide formation is hindered by large activation barriers, compared to the ones involved for acrolein formation. We must remark, however, that the process of hydrogen abstraction from the propene methyl group involves the presence of two neighbouring oxygen adatoms (one being involved in the propene oxametallacycle formation, and another one reacting with the $-CH_3$ group), suggesting that moderate oxygen coverages are necessary to make this process feasible. On silver nanoparticle edges, we find a similar preference for acrolein formation, although the difference in reaction barrier heights for both processes is now much smaller.

Above 100 °C we have the formation of surface oxides on the particle surfaces. Unfortunately, the situation is very complex: experiments [55,56,97,111] show that there is probably a mixture of different structures. We can reasonably hypothesize the presence of a substantial number of subsurface oxygen atoms. In our simulations, we find the energy barrier for acrolein formation larger than the barrier for the formation of propylene oxide. This is due to the extensive rearrangements that must take place for H-abstraction on these extended (1 1 1) surfaces. The formation of propene oxametallacycle intermediates involves reaction with oxygen adatoms in the topmost layer, with only subsurface oxygen neighbours. The formation of acrolein must necessarily occur through diffusion of subsurface oxygen species, which requires a large amount of energy. It is important to remark that reaction pathways for acrolein formation involving direct reaction of adsorbed propene with neigbouring oxygen surface adatoms were also studied, but the barriers involved were even larger; from this fact, an important conclusion can be reached: the OMC complex serves as a reaction intermediate for both propylene oxide and acrolein formation. Therefore we can conclude that in the case of large particles, where such extended surfaces are dominant, PO desorption becomes competitive with H-abstraction and hence the PO/acrolein ratio strongly increases above 100 °C, in agreement with experimental observations. For the smaller particles, the greater presence of edges, kinks, defects in general, probably implies a more irregular oxygen distribution making that oxygen atoms are still (at least in part) available for H-abstraction. PO formation in the final products hence increases but does not become dominant. Upon modelling a small oxidized Ag nanoparticle (see insets in Fig. 17), we find a strong stability for oxygen adatoms placed at both sides of the nanoparticle edge. The existence of such special arrangement allows now for reduced energy barriers in the process leading to acrolein formation, which effectively results in a reduced PO/acrolein ratio, in agreement with experimental observations.

In passing we note that the reaction mechanisms by very small, sub-nanometer size clusters can be very different from those occurring on few-nanometer particles or extended surfaces. The presence of a dominant number of under-coordinated sites is in fact known to modify substantially the chemistry of these systems [23,25,26,116]. These concepts have been refined by a more detailed analysis of the cluster frontier orbitals, from which basic principles for alkene epoxidation by very small Au clusters have been derived by Metiu and co-workers [34], while the question of the relevance of surface defectivity on the cluster catalytic activity has also been the subject of some attention, see e.g. Ref. [117]. It is also important to note that this study was focused on the catalytic oxidation of propene to propylene oxide with molecular oxygen, in the absence of any additives or promoters. The only co-product observed was acrolein, another valuable commodity chemical. Our results show that by proper choice of the size of the silver clusters either propylene oxide or acrolein can be efficiently produced, with high selectivity and under mild reaction conditions.

## 6. Summary

Highly monodispersed model silver nanocatalyst with three average lateral diameters (23.3, 12, and 8.7 nm) were prepared by size-selected cluster deposition on amorphous alumina films and their size-dependent catalytic performance was studied for the partial oxidation of propylene under realistic reaction conditions. All clusters tested were very stable up to 200 °C, without any signs of sintering under reaction conditions. Smaller clusters (8.7 and 12 nm) preferentially produced acrolein, while the 23.3 nm large particles were considerably more selective towards the formation of propylene oxide. The observed reaction rates considerably exceeded previously reported rates for larger silver particles. The activity of clusters dropped significantly with increasing particle size, with an about order of magnitude change in the ratio between propylene oxide and acrolein produced. The different specificities and temperature dependences of the TOR for the smaller versus the larger clusters studied indicate a change in reaction mechanism as a function of size.

Using HRETEM and GISAXS, the surface crystallinity of the clusters were investigated both in vacuum and under realistic catalytic conditions. These results indicate a changing surface crystal structure for the particles under reaction conditions. Density-functional calculations of the activation energies for oxygen adsorption and its dissociation, at variable surface coverages on each silver plane yielded surface energies which resulted in particle shapes consistent with experimentally observed morphologies of the partially oxidized silver clusters. Moreover, the changing crystal plane stabilities are consistent with particle shape changes due to changing plane areas.

The activation barriers calculated for the formation of propylene oxide and acrolein on various facets and on the edges of the silver clusters provided detailed insights into the competing reaction pathways leading to the size/morphology dependent theoretical activity and selectivity, in good agreement with experimental observations. The combined experimental and theoretical results point towards a new class of highly selective silver-based partial oxidation catalysts that works under mild reaction conditions and with molecular oxygen.

## Acknowledgements

The work at Universidad de Valladolid was supported by Ministerio de Ciencia e Innovación (MAT2008-06483-C03-01 project) and Junta de Castilla y León (VA017A08 and GR23 projects). LMM acknowledges fruitful discussions with Paulina Martin. The work at IPCF-CNR was supported by the EC VII FP within the ERC-AG SEPON project (ERC-2008-AdG-227457) and the computational support by the CASPUR Supercomputing Center (Rome, Italy) within the "Competitive HPC Grant 2009" E-MOON project. The work at the Universität Rostock was supported by the Deutsche Forschungsgemeinschaft, Schwerpunktprogramm 1153 "Cluster in Kontakt mit Oberflächen" (German Science Foundation, Priority Program "Clusters at Surfaces"). Y.L. and R.J.M would like to acknowledge support from the American Chemical Society Petroleum Research Fund. The work at Argonne National Laboratory was supported by the US Department of Energy, BES-Materials Sciences and BES-Chemical Sciences, and BES-Scientific User Facilities under Contract DE-AC-02-06CH11357 with UChicago Argonne, LLC, Operator of Argonne National Laboratory. S.V. gratefully acknowledges the support by the Air Force Office of Scientific Research.

## References

[1] T.A. Nijhuis, M. Makkee, J.A. Moulijn, B.M. Weckhuysen, Ind. Eng. Chem. Res. 45 (2006) 3447–3459.
[2] F.W. Zemichael, A. Palermo, M.S. Tikhov, R.M. Lambert, Catal. Lett. 80 (2002) 93–98.
[3] R.M. Lambert, F.J. Williams, R.L. Cropley, A. Palermo, J. Mol. Catal. A: Chem. 228 (2005) 27–33.
[4] H.-J.A.K. Weissermel, Industrial Organic Chemistry, Wiley-VCH, Weinheim, Germany, 2003.
[5] J.Q. Lu, J.J. Bravo-Suarez, A. Takahashi, M. Haruta, S.T. Oyama, J. Catal. 232 (2005) 85–95.
[6] T.A.R. Nijhuis, T. Visser, B.M. Weckhuysen, Angew. Chem. Int. Ed. 44 (2005) 1115–1118.
[7] T. Hayashi, K. Tanaka, M. Haruta, J. Catal. 178 (1998) 566–575.
[8] M.F. Luo, J.Q. Lu, C. Li, Catal. Lett. 86 (2003) 43–49.
[9] W. Yao, Y.L. Guo, X.H. Liu, Y. Guo, Y.Q. Wang, Y.S. Wang, Z.G. Zhang, G.Z. Lu, Catal. Lett. 119 (2007) 185–190.
[10] J.G. Serafin, A.C. Liu, S.R. Seyedmonir, J. Mol. Catal. A: Chem. (1998) 157–168.
[11] J.T. Ranney, S.R. Bare, Surf. Sci. 382 (1997) 266–274.
[12] M.A. Barteau, R.J. Madix, J. Am. Chem. Soc. 105 (1983) 344–349.
[13] D.M. Cox, B. Kessler, P. Fayet, W. Eberhardt, Z. Fu, D. Sondericher, R. Sherwood, A. Kaldor, Nanostruct. Mater. 1 (1992) 161–165.
[14] T. Leisner, C. Rosche, S. Wolf, F. Granzer, L. Woeste, Surf. Rev. Lett. 3 (1996) 1105–1108.
[15] F. Vanolli, U. Heiz, W.-D. Schneider, Chem. Phys. Lett. 277 (1997) 527–531.
[16] W. Bouwen, E. Kunnen, K. Temst, P. Thoen, M.J. Van Bael, F. Vanhoutte, H. Weidele, P. Lievens, R.E. Silverans, Thin Solid Films 354 (1999) 87–92.
[17] S.J. Carroll, S. Pratontep, M. Steun, R.E. Palmer, S. Hobday, R. Smith, J. Chem. Phys. 113 (2000) 7723–7727.
[18] R.P. Methling, V. Senz, E.-D. Klinkenberg, T. Diederich, J. Tiggesbaumker, G. Holzhuter, J. Bansmann, K.H. Meiwes-Broer, Eur. Phys. J. D 16 (2001) 173–176.
[19] K. Judai, A.S. Wörz, S. Abbet, U. Heiz, J. Am. Chem. Soc. 126 (2004) 2732–2737.
[20] S. Lee, C. Fan, T. Wu, S.L. Anderson, J. Chem. Phys. 123 (2005), 124710-1-13.
[21] D.C. Lim, R. Dietsche, M. Bubek, G. Gantefor, Y.D. Kim, ChemPhysChem 7 (2006) 1909–1911.
[22] S. Vajda, R.E. Winans, J.W. Elam, B.D. Lee, M.J. Pellin, S. Seifert, G.Y. Tikhonov, N.A. Tomczyk, Top. Catal. 39 (2006) 161–166.
[23] S. Lee, L.M. Molina, M.J. López, J.A. Alonso, B. Hammer, B. Lee, S. Seifert, R.E. Winans, J.W. Elam, M.J. Pellin, S. Vajda, Angew. Chem. Int. Ed. 48 (2009) 1467–1471.
[24] S. Vajda, S. Lee, K. Sell, I. Barke, A. Kleibert, V. von Oeynhausen, K.H. Meiwes-Broer, A.F. Rodriguez, J.W. Elam, M.J. Pellin, B. Lee, S. Seifert, R.E. Winans, J. Chem. Phys. 131 (2009), 121104-1-7.
[25] Y. Lei, F. Mehmood, S. Lee, J.P. Greeley, B. Lee, S. Seifert, R.E. Winans, J.W. Elam, R.J. Meyer, P.C. Redfern, D. Teschner, R. Schlögl, M.J. Pellin, L.A. Curtiss, S. Vajda, Science 328 (2010) 224–228.
[26] S. Vajda, M.J. Pellin, J.P. Greeley, C.L. Marshall, L.A. Curtiss, G.A. Ballentine, J.W. Elam, S. Catillon-Mucherie, P.C. Redfern, F. Mehmood, P. Zapol, Nat. Mater. 8 (2009) 213–216.
[27] Z. Xu, F.S. Xiao, S.K. Purnell, O. Alexeev, S. Kawi, S.E. Deutsch, B.C. Gates, Nature 372 (1994) 346–348.
[28] X. Tong, L. Benz, P. Kemper, H. Metiu, M.T. Bowers, S.K. Buratto, J. Am. Chem. Soc. 127 (2005) 13516–13518.
[29] K. Bromann, C. Felix, H. Brune, W. Harbich, R. Monot, J. Buttet, K. Kern, Science 274 (1996) 956–958.
[30] M.S. Chen, D.W. Goodman, Science 306 (2004) 252–255.
[31] C. Lemire, R. Meyer, S. Shaikhutdinov, H.-J. Freund, Angew. Chem. Int. Ed. 43 (2004) 118–121.
[32] A.T. Bell, Science 299 (2003) 1688–1691.
[33] F. Tao, M.E. Grass, Y. Zhang, D.R. Butcher, J.R. Renzas, Z. Liu, J.Y. Chung, B.S. Mun, M. Salmeron, G.A. Somorjai, Science 322 (2008) 932–934.
[34] S. Chrétien, S.K. Buratto, H. Metiu, Curr. Solid Opin. St. M. 11 (2007) 62–75.
[35] L. Benz, X. Tong, P. Kemper, Y. Lilach, A. Kolmakov, H. Metiu, T. Bowers Michael, K. Buratto Steven, J. Chem. Phys. 122 (2005), 81102-1-4.
[36] U. Heiz, U. Landman (Eds.), Nanocatalysis, Springer-Verlag, Berlin, Heidelberg, New York, 2007 (ISBN-13 978-3-540-32645-8).
[37] B. Yoon, H. Häkkinen, U. Landman, A.S. Wörz, J.-M. Antonietti, S. Abbet, K. Judai, U. Heiz, Science 307 (2005) 403–407.
[38] S. Lee, C. Fan, T. Wu, S.L. Anderson, J. Phys. Chem. B 109 (2005) 11340–11347.
[39] S. Lee, C. Fan, T. Wu, S.L. Anderson, J. Am. Chem. Soc. 126 (2004) 5683–5684.
[40] M. Aizawa, S. Lee, S.L. Anderson, Surf. Sci. 542 (2003) 253–275.
[41] S. Lee, B. Lee, F. Mehmood, S. Seifert, J.A. Libera, J.W. Elam, J. Greeley, P. Zapol, L.A. Curtiss, M.J. Pellin, P.C. Stair, R.E. Winans, S. Vajda, J. Phys. Chem. C 114 (2010) 10342–10348.
[42] K. Luo, X. Lai, C.W. Yi, K.A. Davis, K.K. Gath, D.W. Goodman, J. Phys. Chem. B 109 (2005) 4064–4068.
[43] A.L. de Oliveira, A. Wolf, F. Schuth, Catal. Lett. 73 (2001) 157–160.
[44] G. Renaud, R. Lazzari, C. Revenant, A. Barbier, M. Noblet, O. Ulrich, F. Leroy, J. Jupille, Y. Borensztein, C.R. Henry, J.-P. Deville, F. Scheurer, J. Mane-Mane, O. Fruchart, Science 300 (2003) 1416–1419.
[45] R.E. Winans, S. Vajda, B. Lee, S.J. Riley, S. Seifert, G.Y. Tikhonov, N.A. Tomczyk, J. Phys. Chem. B 108 (2004) 18105.
[46] S.A. Wyrzgol, S. Schäfer, S. Lee, B. Lee, M. Di Vece, X. Li, S. Seifert, R.E. Winans, M. Stutzmann, J.A. Lercher, S. Vajda, Phys. Chem. Chem. Phys. (2010) 5585–5595.
[47] G. Cipriani, D. Loffreda, A. Dal Corso, S. de Gironcoli, S. Baroni, Surf. Sci. 501 (2002) 182.
[48] A. Kokalj, A.D. Corso, S.D. Gironcoli, S. Baroni, Surf. Sci. 532–535 (2003) 191–197.
[49] A. Kokalj, A. Dal Corso, S. de Gironcoli, S. Baroni, Surf. Sci. 507–510 (2002) 62–68.
[50] A. Kokalj, A. Dal Corso, S. de Gironcoli, S. Baroni, J. Phys. Chem. B 106 (2002) 9839–9846.
[51] A. Kokalj, A. Dal Corso, S. de Gironcoli, S. Baroni, Surf. Sci. 566–568 (2004) 1018–1023.
[52] A. Kokalj, P. Gava, S. de Gironcoli, S. Baroni, J. Phys. Chem. C 112 (2008) 1019–1027.
[53] S. Linic, M.A. Barteau, J. Am. Chem. Soc. 125 (2003) 4034–4035.
[54] M.-L. Bocquet, A. Michaelides, D. Loffreda, P. Sautet, A. Alavi, D.A. King, J. Am. Chem. Soc. 125 (2003) 5620–5621.
[55] M. Schmid, A. Reicho, A. Stierle, I. Costina, J. Klikovits, P. Kostelnik, O. Dubay, G. Kresse, J. Gustafson, E. Lundgren, J.N. Andersen, H. Dosch, P. Varga, Phys. Rev. Lett. 96 (2006), 146102-1-4.
[56] J. Schnadt, A. Michaelides, J. Knudsen, R.T. Vang, K. Reuter, E. Laegsgaard, M. Scheffler, F. Besenbacher, Phys. Rev. Lett. 96 (2006), 146101-1-4.
[57] A.W. Ott, J.W. Klaus, J.M. Johnson, S.M. George, Thin Solid Films 292 (1997) 135–144.
[58] J. Passig, K.-H. Meiwes-Broer, J. Tiggesbäumker, Rev. Sci. Instrum. 77 (2006), 093304-1-5.
[59] R. Schaub, H. Jödicke, F. Brunet, R. Monot, J. Buttet, W. Harbich, Phys. Rev. Lett. 86 (2001) 2590–2593.
[60] W. Harbich, Philos. Magn. B 79 (1999) 1307–1320.
[61] U. Heiz, W.-D. Schneider, J. Phys. D: Appl. Phys. 33 (2000) R85–R102.
[62] H.-P. Cheng, U. Landman, Science 260 (1993) 1304–1307.
[63] M.O. Watanabe, N. Uchida, T. Kanayama, Phys. Rev. B 61 (2000) 7219–7222.
[64] M. Getzlaff, A. Kleibert, R. Methling, J. Bansmann, K.-H. Meiwes-Broer, Surf. Sci. 566–568 (2004) 332–336.
[65] A. Kleibert, A. Voitkans, K.H. Meiwes-Broer, Phys. Rev. B 81 (2010), 073412-1-4.
[66] S. Giorgio, S.S. Joao, S. Nitsche, D. Chaudanson, G. Sitja, C.R. Henry, Ultramicroscopy 106 (2006) 503–507.
[67] P.L. Gai, E.D. Boyes, S. Helveg, P.L. Hansen, S. Giorgio, C.R. Henry, MRS Bull. 32 (2007) 1044–1050.
[68] B. Lee, S. Seifert, S.J. Riley, G.Y. Tikhonov, N.A. Tomczyk, S. Vajda, R.E. Winans, J. Chem. Phys. 123 (2005), 074701-1-7.
[69] S. Vajda, R.E. Winans, J.W. Elam, B. Lee, M.J. Pellin, S.J. Riley, S. Seifert, G.Y. Tikhonov, N.A. Tomczyk, Prepr. Am. Chem. Soc. Div. Fuel Chem. 50 (2005) 190–191.
[70] S. Vajda, G.P. Wiederrecht, A. Bouhelier, G.Y. Tikhonov, N. Tomczyk, B. Lee, S. Seifert, R.E. Winans, Collect. Czech. Chem. C 72 (2007) 121–128.

[71] A. Barbier, G. Renaud, J. Jupille, Surf. Sci. 454–456 (2000) 979–983.
[72] R.E. Winans, S. Vajda, G.E. Ballentine, J.W. Elam, B.D. Lee, M.J. Pellin, S. Seifert, G.Y. Tikhonov, N.A. Tomczyk, Top. Catal. 39 (2006) 145–149.
[73] R. Wengeler, F. Wolf, N. Dingenouts, H. Nirschl, Langmuir 23 (2007) 4148–4154.
[74] A. Turkovic, Mater. Sci. Eng. B: Solid B 75 (2000) 85–91.
[75] A. Guinier, G. Fournet, C.B. Walker, K.L. Yudowitch, Small Angle Scattering of X-Rays, Wiley, New York, 1955.
[76] J.T. Ranney, S.R. Bare, J.L. Gland, Catal. Lett. 48 (1997) 25–29.
[77] K.A. Davis, D.W. Goodman, J. Phys. Chem. B 104 (2000) 8557–8562.
[78] J. Chou, E.W. McFarland, Chem. Commun. (2004) 1648–1649.
[79] T.A. Nijhuis, E. Sacaliuc-Parvulescu, N.S. Govender, J.C. Schouten, B.M. Weckhuysen, J. Catal. 265 (2009) 161–169.
[80] W.X. Huang, J.M. White, Catal. Lett. 84 (2002) 143–146.
[81] W.E. Kaden, T. Wu, W.A. Kunkel, S.L. Anderson, Science 326 (2009) 826–829.
[82] S. Orisaka, T. Minobe, T. Uchihashi, Y. Sugawara, S. Morita, Appl. Surf. Sci. 140 (1999) 243–246.
[83] P. Giannozzi, S. Baroni, N. Bonini, M. Calandra, R. Car, C. Cavazzoni, D. Ceresoli, G.L. Chiarotti, M. Cococcioni, I. Dabo, A. Dal Corso, S. de Gironcoli, S. Fabris, G. Fratesi, R. Gebauer, U. Gerstmann, C. Gougoussis, A. Kokalj, M. Lazzeri, L. Martin-Samos, N. Marzari, F. Mauri, R. Mazzarello, S. Paolini, A. Pasquarello, L. Paulatto, C. Sbraccia, S. Scandolo, G. Sclauzero, A.P. Seitsonen, A. Smogunov, P. Umari, R.M. Wentzcovitch, J. Phys. Condens. Mater. 21 (2009), 395502-1-18.
[84] D. Vanderbilt, Phys. Rev. B 41 (1990) 7892–7895.
[85] J.P. Perdew, K. Burke, M. Ernzerhof, Phys. Rev. Lett. 77 (1996) 3865–3868.
[86] DACAPO, See DACAPO web page at Danish Technical University: https://wiki.fysik.dtu.dc/dacapo.
[87] J.P. Perdew, J.A. Chevary, S.H. Vosko, K.A. Jackson, M.R. Pederson, D.J. Singh, C. Fiolhais, Phys. Rev. B 46 (1992) 6671–6687.
[88] A. Alavi, P. Hu, T. Deutsch, P.L. Silvestrelli, J. Hutter, Phys. Rev. Lett. 80 (1998) 3650–3653.
[89] A.K. Santra, B.K. Min, D.W. Goodman, Surf. Sci. 515 (2002) L475–L479.
[90] M. Rocca, L. Vattuone, L. Savio, F.B.D. Mongeot, U. Valbusa, G. Comelli, S. Lizzit, A. Baraldi, G. Paolucci, J.A. Groeneveld, E.J. Baerends, Phys. Rev. B 63 (2001), 081404-1-4.
[91] V.I. Bukhtiyarov, V.V. Kaichev, J. Mol. Catal. A: Chem. 158 (2000) 167–172.
[92] C.T. Campbell, Surf. Sci. 157 (1985) 43–60.
[93] L. Savio, L. Vattuone, M. Rocca, Appl. Phys. A: Mater. 87 (2007) 399–404.
[94] A. Takahashi, N. Hamakawa, I. Nakamura, T. Fujitani, Appl. Catal. A: Gen. 294 (2005) 34–39.
[95] F. Buatier de Mongeot, A. Cupolillo, M. Rocca, U. Valbusa, Chem. Phys. Lett. 302 (1999) 302–306.
[96] A. Michaelides, K. Reuter, M. Scheffler, J. Vac. Sci. Technol. A 23 (2005) 1487.
[97] W.X. Li, C. Stampfl, M. Scheffler, Phys. Rev. B 67 (2003), 045408-1-16.
[98] D.S. Su, T. Jacob, T.W. Hansen, D. Wang, R. Schlögl, B. Freitag, S. Kujawa, Angew. Chem. Int. Ed. 47 (2008) 5005.
[99] A.J. Nagy, G. Mestl, R. Schlögl, J. Catal. 188 (1999) 58–68.
[100] A. Reicho, A. Stierle, I. Costina, H. Dosch, Surf. Sci. 601 (2007) L19–23.
[101] L. Vitos, A.V. Ruban, H.L. Skriver, J. Kollár, Surf. Sci. 411 (1998) 186–202.
[102] S. Giorgio, M. Cabie, C.R. Henry, Gold Bull. 41 (2008) 167–173.
[103] M. Cabie, S. Giorgio, C.R. Henry, M.R. Axet, K. Philippot, B. Chaudret, J. Phys. Chem. C 114 (2010) 2160–2163.
[104] S. Giorgio, C.R. Henry, B. Pauwels, G. Van Tendeloo, Mater. Sci. Eng. A: Struct. 297 (2001) 197–202.
[105] S. Giorgio, C.R. Henry, C. Chapon, G. Nihoul, J.M. Penisson, Ultramicroscopy 38 (1991) 1–12.
[106] T. David, D. Buttard, T. Schülli, F. Dallhuin, P. Gentile, Surf. Sci. 602 (2008) 2675–2680.
[107] M.-L. Bocquet, P. Sautet, J. Cerda, C.I. Carlisle, M.J. Webb, D.A. King, J. Am. Chem. Soc. 125 (2003) 3119–3125.
[108] A. Kokalj, A. Dal Corso, S. de Gironcoli, S. Baroni, J. Phys. Chem. B 110 (2006) 367–376.
[109] C.I. Carlisle, T. Fujimoto, W.S. Sim, D.A. King, Surf. Sci. 470 (2000) 15–31.
[110] R. Ferrando, G. Rossi, A.C. Levi, Z. Kuntova, F. Nita, A. Jelea, C. Mottet, G. Barcaro, A. Fortunelli, J. Goniakowski, J. Chem. Phys. 130 (2009) 174702-1-9.
[111] I. Costina, M. Schmid, H. Schiechl, M. Gajdos, A. Stierle, S. Kumaragurubaran, J. Hafner, H. Dosch, P. Varga, Surf. Sci. 600 (2006) 617–624.
[112] M.-L. Bocquet, D. Loffreda, J. Am. Chem. Soc. 127 (2005) 17207–17215.
[113] S. Linic, M.A. Barteau, J. Am. Chem. Soc. 124 (2001) 310–317.
[114] S. Linic, H. Piao, K. Adib, M.A. Barteau, Angew. Chem. Int. Ed. 43 (2004) 2918–2921.
[115] J. Greeley, M. Mavrikakis, J. Phys. Chem. C 111 (2007) 7992–7999.
[116] N. Lopez, T.V.W. Janssens, B.S. Clausen, Y. Xu, M. Mavrikakis, T. Bligaard, J.K. Nørskov, J. Catal. 223 (2004) 232–235.
[117] A.M. Joshi, W.N. Delgass, K.T. Thomson, J. Phys. Chem. C 111 (2007) 7841–7844.